

ÉCOLE NORMALE SUPÉRIEURE
PRINCETON PLASMA PHYSICS LABORATORY

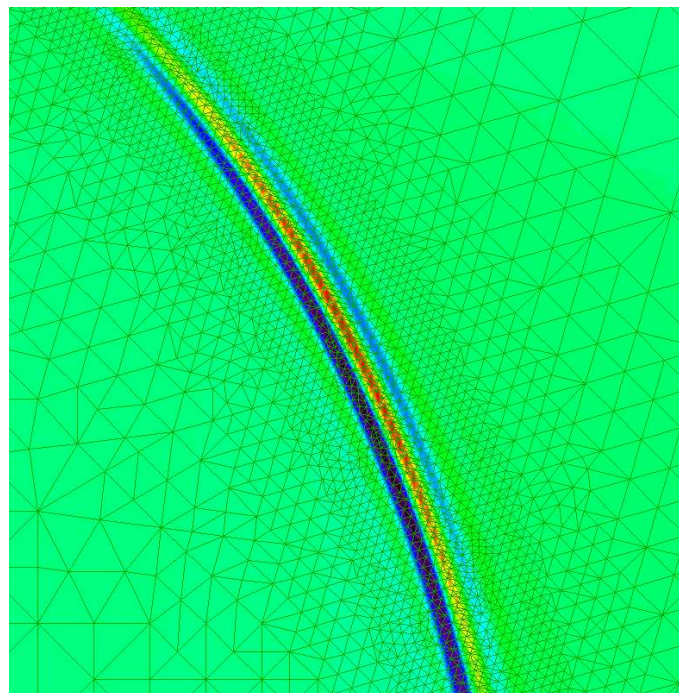
STAGE LONG DE RECHERCHE, FIP M1
SECOND SEMESTRE 2010-2011

Stability study of the cylindrical tokamak

Étude de stabilité du tokamak cylindrique

Author:
Thomas SCAFFIDI

Supervisor:
Prof. Stephen C. JARDIN



Abstract

Une des instabilités les plus problématiques dans les plasmas de tokamak est appelée *tearing mode*. Elle est générée par les gradients de courant et de pression et implique une reconfiguration du champ magnétique et du champ de vitesse localisée dans une fine région autour d'une surface magnétique résonante. Alors que les lignes de champ magnétique sont à l'équilibre situées sur des surfaces toriques concentriques, l'instabilité conduit à la formation d'îles magnétiques dans lesquelles les lignes de champ passent d'un tube de flux à l'autre, rendant possible un transport thermique radial important et donc créant une perte de confinement. Pour qu'il puisse y avoir une reconfiguration du champ magnétique, il faut inclure la résistivité du plasma dans le modèle, et nous résolvons donc les équations de la magnétohydrodynamique (MHD) résistive. On s'intéresse à la stabilité de configurations d'équilibre vis-à-vis de ces instabilités dans un système à la géométrie simplifiée appelé le tokamak cylindrique. L'étude est à la fois analytique et numérique. La solution analytique est réalisée par une méthode de type "couche limite" qui tire profit de l'étroitesse de la zone où la reconfiguration a lieu. On peut en effet négliger la résistivité partout sauf dans cette zone. On obtient donc deux solutions, extérieure et intérieure, et leur raccordement nous donne le taux de croissance de l'instabilité et la dépendance spatiale du mode. La solution numérique est obtenue avec un code de type éléments finis d'ordre élevé et implicite appelé M3DC1 et développé au Princeton Plasma Physics Laboratory. Des maillages raffinés au niveau de la couche limite ont du être générés, comme on peut le voir sur l'illustration de la page de garde. Un accord assez bon a pu être montré entre les résultats obtenus via ces deux méthodes, confirmant la capacité du code M3DC1 à effectuer des études de stabilité en MHD résistive.

One of the most problematic instabilities in tokamak plasmas are tearing modes. They are driven by current and pressure gradients and involve a reconfiguration of the magnetic and velocity fields localized into a narrow region located at a resonant magnetic surface. While the equilibrium magnetic field lines are located on concentric toroidal surfaces, the instability creates magnetic islands in which field lines connect flux tubes together, allowing for a high radial heat transport, and thus creating a loss of confinement. In order for the magnetic field to break field lines and reconnect, we need to take into account the resistivity of the plasma, and thus we solve the resistive magnetohydrodynamics (MHD) equations. The linear stability of typical tokamak equilibria against these instabilities were studied in a test case called the cylindrical tokamak with both analytical and numerical tools. The analytical solution consists in a boundary layer analysis (asymptotic matching) and takes advantage of the small radial width of the region where the perturbations vary significantly. Indeed, ideal magnetohydrodynamics can be used everywhere except in that narrow region where the full resistive problem must be solved. The numerical solution was obtained with an implicit high-order finite elements code called M3DC1 and developed at Princeton Plasma Physics Laboratory. Adaptive meshes had to be generated to be able to capture the sharp spatial gradients in the boundary layer. A fairly good agreement is shown between both solutions, confirming the linear resistive capabilities of M3DC1.

Acknowledgements

Foremost, I would like to express my sincere gratitude to my advisor Prof. Stephen Jardin for offering me the opportunity to work on an exciting project in the best conditions, and for the continuous support of my research and my life in Princeton in general. He was always ready to help and every discussion we had was inspiring and motivating. I want to thank him for the trust he has placed in me at all times and especially by giving me the chance to attend the Sherwood conference.

I also want to thank Stuart Hudson, Jin Chen, Nate Ferraro, Joshua Breslau, Fabien Delalondre and Kevin Ying for their constant help, support and time.

I am grateful to my fellow labmates : Pierre Baele, Daniel Ruiz, Derek Thompson, Jean-Carlos Gayoso, Steve DePasquale, Brendan Lyons, C. Lee Ellison and Enrique Merino for the sleepless nights we were working (or not) before deadlines, and for all the fun we had during these six months.

Last but not the least, I would like to thank Céline, my parents and my brothers, who have always shown me unconditional support and to whom I owe everything.

Contents

1	Introduction	4
2	The Cylindrical Tokamak	5
2.1	Equilibrium	6
3	Linear Stability	8
3.1	Ideal Stability	9
3.1.1	Preliminary results	9
3.1.2	Stability condition	11
3.2	Resistive Stability - Asymptotic Matching	14
3.2.1	Outer Region	15
3.2.2	Inner Region	18
3.2.3	Matching	21
4	The M3DC1 code	23
4.1	Temporal discretization	23
4.2	Spatial discretization	24
4.3	Implementation of the cylindrical tokamak	27
5	Benchmark	27
6	Conclusion	28
A	Appendix	31
A.1	“Frozen in” theorem	31
A.2	Parity conservation	32
A.3	Figures	33

1 Introduction

I give here a report of the work I have done at the Princeton Plasma Physics Laboratory (PPPL). This lab has been working on plasma physics to develop nuclear fusion as a clean energy source since the very beginning of the field in the fifties. Since then, several reactor designs using magnetic confinement were proposed and studied both theoretically and experimentally : tokamak (on which the present report focuses), stellarator, spheromak, spherical tokamak, reversed field pinch... The tokamak and the stellarator are the most promising devices at the moment and most of the fusion community effort is dedicated to them, notably with the construction of respectively ITER in France and Wendelstein 7-X in Germany.

Let us start with a brief summary of nuclear fusion. The idea is to use the energy released when a deuterium and a tritium nuclei fuse into an helium nucleus and a neutron. In order to make them fuse, the temperature has to be high enough so as to overcome the repulsive Coulomb potential between the two positive nuclei. Indeed, the cross section of the fusion nuclear reaction has a peak around 50 keV, i.e. 10^8 K. At that temperature the plasma is fully ionized and can thus be confined magnetically. If we neglect the Larmor radius, charged particles follow magnetic field lines and we then need a magnetic configuration for which field lines stay in a closed volume to assure confinement of the plasma. Because of the divergence free nature of the magnetic field, the simplest of such topological configurations is the torus[18], and this is why the tokamak is a toroidal reactor.

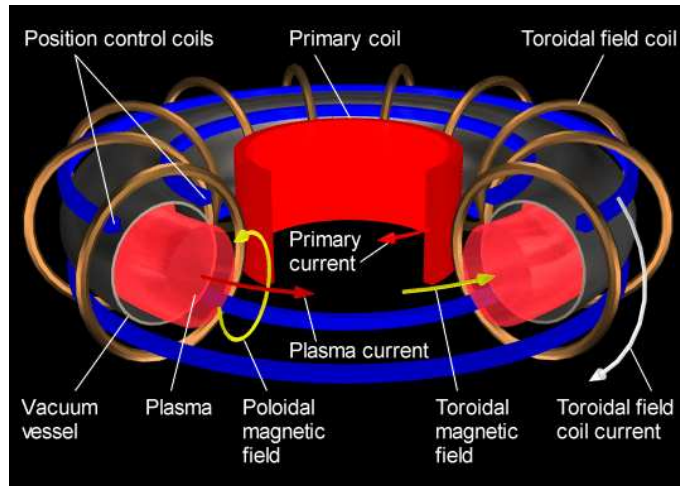


Figure 1: Cartoon of a tokamak (Courtesy of <http://www.plasma.inpe.br>)

The major component of the magnetic field is toroidal and is produced by the poloidal current in the toroidal field coils (see Fig. 1). A toroidal current is driven through the plasma with the primary coil. This current generates the poloidal magnetic field and heats the plasma due to its resistivity (Ohmic heating). Unfortunately, the resistivity of the plasma decreases with temperature and thus the Ohmic heating is not sufficient to reach the desired temperature. Auxiliary heating is therefore needed and achieved by two main methods : high-energy neutral beam injection and radio-frequency waves.

In order to reach ignition of the plasma, i.e. a self-sustained burning plasma, we need to have the largest pressure and temperature possible, and for the longest discharge time possible. There are a lot of instabilities which appear in the plasma when these parameters get large. In the best case they only reduce confinement by permitting transport of particles or energy outward, in the

worst case they cause disruption, which is a sudden total loss of confinement. Thus we need a model to predict operational limits imposed by these instabilities.

We can distinguish two types of model for plasmas : fluid models, which describe only the first moments of the particle velocity distribution (density, velocity, kinetic energy) and kinetic models, which describe the full particle velocity distribution. Fluid models are valid when the collisionality is high enough so that the particle velocity distribution is Maxwellian. The simplest of the fluid models is Ideal MagnetoHydroDynamics (MHD), which is basically the Euler equations and the Maxwell equations coupled by the $\vec{J} \times \vec{B}$ force and Ohm's law. The first dissipative effect to be taken into account to have a realistic model of a plasma is its finite resistivity, and we then obtain Resistive MagnetoHydroDynamics.

One possible approach to solve the Partial Differential Equations (PDE) of MHD is to use a Finite Elements method. My work has consisted in benchmarking a MHD Finite Elements code called M3D-C1 on a test system for which we have an analytic solution using asymptotic matching. I will first describe the test system, the cylindrical tokamak, and the asymptotic matching solution. Then the M3DC1 code will be presented, with an emphasis of how it could be applied to the test system. I will finally show a good agreement between the results of the analytic solution and M3DC1.

2 The Cylindrical Tokamak

In the large aspect ratio limit (the aspect ratio is the ratio of the major radius over the minor one), a tokamak can be seen as a cylinder with periodic boundary conditions in the axial direction because the toroidal curvature can be neglected compared to the poloidal one. This system is called the cylindrical tokamak and has been shown to be very valuable in predicting MHD stability, even for finite aspect ratio tokamaks. To sum up, instead of solving the resistive MHD equations in a torus of major radius R and minor radius a , we solve them in a cylinder with radius a and length $2\pi R$. This is the reason why, in the following, even though we will only work in cylindrical geometry, we will sometimes use the words "poloidal" (torus) instead of "circumferential" (cylinder) and "toroidal" (torus) instead of "axial" (cylinder).

The minor radius a is taken to be one or equivalently all the lengths are normalized by the minor radius. The tokamak wall is assumed to be a perfect conductor, imposing the radial magnetic field and the tangential electric field to be zero at $r = 1$. The radial velocity must vanish at the edge as well for obvious reason. There is no boundary condition on the tangential velocity because we assume no viscosity.

Here are the equations of resistive MHD :

$$\begin{aligned}\frac{\partial \rho}{\partial t} + \nabla \cdot (\rho \vec{v}) &= 0 \\ \frac{\partial \vec{v}}{\partial t} + \vec{v} \cdot \nabla \vec{v} &= -\frac{1}{\rho} \nabla p + \frac{1}{\rho} \vec{J} \times \vec{B} \\ \frac{\partial p}{\partial t} + \vec{v} \cdot \nabla p + \Gamma p \nabla \cdot \vec{v} &= (\Gamma - 1) \eta \vec{J}^2 \\ \frac{\partial \vec{B}}{\partial t} &= -\nabla \times \vec{E} \\ \vec{E} + \vec{v} \times \vec{B} &= \eta \vec{J} \\ \vec{J} &= \nabla \times \vec{B}\end{aligned}$$

with Γ the adiabatic index and η the electrical resistivity of the plasma. These are respectively the conservation of mass, the conservation of momentum (the electric field exerts no force because we assume quasi-neutrality of the plasma), the conservation of internal energy where the adiabatic assumption has been made, Faraday's law, Ohm's law in a moving frame and Ampère's law where the displacement current has been neglected (non-relativistic approximation). Throughout this text we use rationalized units for which $\mu_0 = 1$, which means that p in these equations must be understood as the pressure in Pascal times $\mu_0 = 4\pi 10^{-7} [V \cdot s / (A \cdot m)]$, that ρ must be understood as the density in kilograms per cube metre times μ_0 , that η must be understood as the resistivity in Ohm metre divided by μ_0 and that \vec{J} must be understood as the current density in amperes per square metre times μ_0 .

2.1 Equilibrium

We are interested in axisymmetric flow-less equilibria. By setting ∂_t and \vec{v} to 0 and by neglecting the resistive terms, we obtain

$$\nabla p = \vec{J} \times \vec{B}$$

Assuming only radial dependance of the equilibrium quantities, the equilibrium equation becomes

$$\frac{dp}{dr} - J_\theta B_z + J_z B_\theta = 0$$

with $J_\theta = -\frac{dB_z}{dr}$, $J_z = \frac{1}{r} \frac{d}{dr} r B_\theta$, $J_r = 0$ and $B_r = 0$. The fact that the radial component of the magnetic field vanishes means that magnetic surfaces are nested concentric cylinders on which magnetic field lines twist (see figure 2).

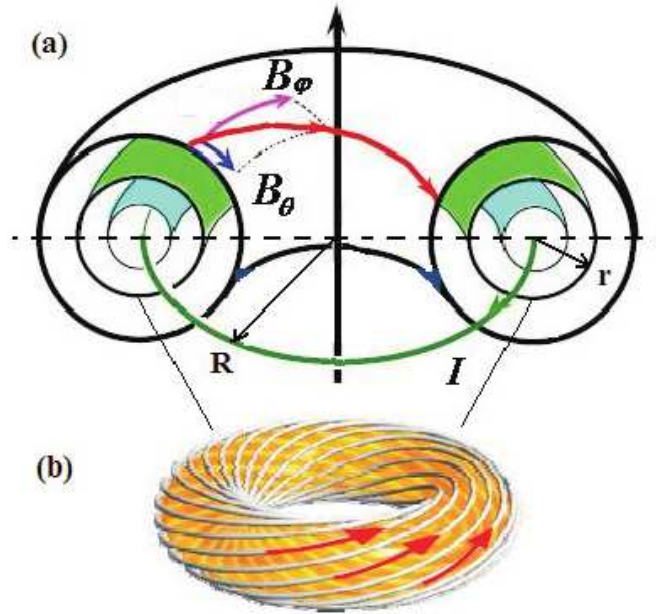


Figure 2: Sketch of magnetic surfaces [3] ($B_\phi \equiv B_z$)

These equilibria are thus defined by two arbitrary radial profiles amongst three (B_z , B_θ and p), the third one being computed with the equilibrium equation. The toroidal current (or equivalently the poloidal magnetic field) and the pressure are often chosen as input. For the poloidal magnetic

field profile, we use the so called “peaked model” defined by Furth, Rutherford and Selberg[14](FRS) because it is well studied and analytically tractable :

$$B_\theta = \hat{B}_\theta \frac{x}{1+x^2}$$

with $x = r/r_0$, r_0 being a measure of the toroidal current channel width. In the FRS paper, only the pressure-less case is treated. We extend this work by adding a parabolic pressure profile :

$$p = \hat{p}(1-r^2)$$

We can now calculate the toroidal magnetic field B_z by integrating the equilibrium equation from the wall at $r = 1$:

$$\frac{d}{dr} \frac{1}{2} B_z^2 = -\frac{dp}{dr} - \frac{B_\theta}{r} \frac{d}{dr} r B_\theta$$

$$B_z = \sqrt{B_z(1)^2 - 2p - 2 \int_1^r \frac{B_\theta}{r'} \frac{d}{dr'} (r' B_\theta) dr'}$$

Using the aforementioned B_θ profile, we find

$$\int_1^r \frac{B_\theta}{r'} \frac{d}{dr'} (r' B_\theta) dr' = \frac{(\hat{B}_\theta)^2}{2} \left(\left(1 + \left(\frac{1}{r_0} \right)^2 \right)^{-2} - \left(1 + \left(\frac{r}{r_0} \right)^2 \right)^{-2} \right)$$

The toroidal magnetic field at the edge $B_z(1)$ is usually normalized to one. It is an experimentally tunable parameter because it is controlled by the current in the coils only and not by the current in the plasma. The remaining equilibrium parameters are thus r_0 , \hat{B}_θ and \hat{p} . We can define a dimensionless number :

$$\beta = \frac{p}{\frac{B_z^2}{2}} = \frac{2\hat{p}}{B_z(1)^2} = 2\hat{p}$$

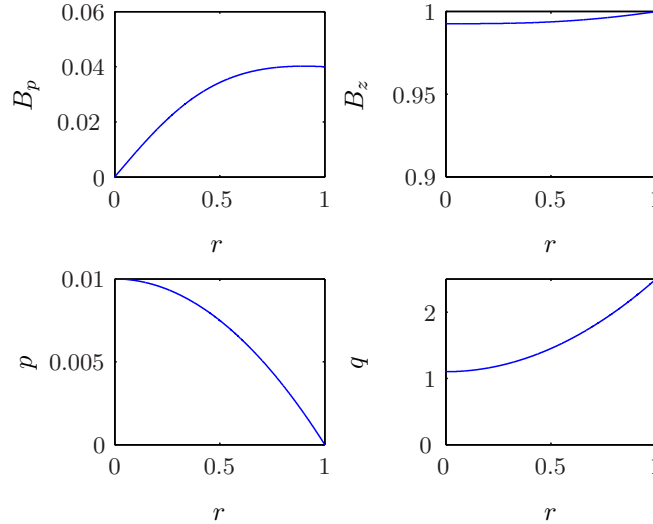


Figure 3: Typical equilibrium profiles. Note that B_z is almost not affected by the plasma and remains close to his imposed value at the edge. The safety factor $q = rB_z/RB_\theta$ is defined in the following.

which is the ratio of the plasma pressure to the magnetic pressure, and which goes approximately from 10^{-3} to 10^{-2} in most tokamaks.

The equilibrium density is assumed uniform and normalized to one.

3 Linear Stability

In order to evaluate the linear stability of such equilibria, we decompose each quantity into an equilibrium and a perturbation part :

$$\begin{aligned}\rho &= \rho_0 + \rho_1(r, \theta, z) \\ \vec{B} &= \vec{B}_0(r) + \vec{B}_1(r, \theta, z) \\ \vec{v} &= \vec{v}_1(r, \theta, z) \\ p &= p_0(r) + p_1(r, \theta, z)\end{aligned}$$

We inject these expressions into the resistive MHD equations and we keep only the terms linear in the perturbation to finally obtain

$$\rho_0 \frac{\partial \vec{v}}{\partial t} = (\nabla \times \vec{B}_0) \times \vec{B}_1 + (\nabla \times \vec{B}_1) \times \vec{B}_0 - \nabla p_1 \quad (1)$$

$$\frac{\partial \vec{B}_1}{\partial t} = \nabla \times (\vec{v} \times \vec{B}_0 - \eta \nabla \times \vec{B}_1) \quad (2)$$

$$\frac{\partial p_1}{\partial t} = -\vec{v} \cdot \nabla p_0 - \Gamma p_0 \nabla \cdot \vec{v} \quad (3)$$

$$\frac{\partial \rho_1}{\partial t} = -\nabla \cdot (\rho_0 \vec{v}) \quad (4)$$

The perturbed density ρ_1 appears only in the last equation and is thus decoupled from the other quantities. We assume an exponential time dependance $e^{\gamma t}$ for all perturbed fields and use the Lagrangian displacement $\vec{\xi} = \frac{1}{\gamma} \vec{v}$ rather than the velocity [2] :

$$\rho_0 \gamma^2 \vec{\xi} = (\nabla \times \vec{B}_0) \times \vec{B}_1 + (\nabla \times \vec{B}_1) \times \vec{B}_0 - \nabla p_1 \quad (5)$$

$$\vec{B}_1 = \nabla \times \left(\vec{\xi} \times \vec{B}_0 - \frac{\eta}{\gamma} \nabla \times \vec{B}_1 \right) \quad (6)$$

$$p_1 = -\vec{\xi} \cdot \nabla p_0 - \Gamma p_0 \nabla \cdot \vec{\xi} \quad (7)$$

This is basically the system of equations we will solve throughout the present paper.

We assume a helical perturbation with m the number of oscillations along 2π in the circumferential (poloidal) direction and n the number of oscillations along $2\pi R = 2\pi/k$ in the axial (toroidal) direction :

$$\vec{\xi} = \vec{\xi}(r) e^{i(m\theta - nkz)}$$

The same spatial dependance is assumed for \vec{B}_1 and p_1 . The system of PDE then simplifies into a system of ODE in the radial direction, r going from 0 (axis) to 1 (boundary).

Notice that the trajectories on which such perturbation field is constant are, for a given r , lines twisting on the cylindrical surface of radius r , just as the equilibrium magnetic field lines shown in figure 2. We have indeed

$$\nabla(m\theta - nkz) = \frac{m}{r} \hat{\theta} - nk \hat{z}$$

and thus if we look for a vector \vec{G} perpendicular to this gradient, we find

$$\vec{G} \propto nk\hat{\theta} + \frac{m}{r}\hat{z}$$

If we define the pitch angle α by the angle between the field line and $\hat{\theta}$, we have for the field lines of \vec{G}

$$\tan(\alpha) = \frac{m}{rnk}$$

while, for the equilibrium magnetic field lines, we have

$$\tan(\alpha) = \frac{B_{z0}}{B_{\theta0}}$$

We can conclude that the field lines will be superposed, or equivalently the perturbation will be constant along equilibrium magnetic field lines, on the cylindrical surface of radius r_s such as

$$\frac{m}{r_s nk} = \frac{B_{z0}(r_s)}{B_{\theta0}(r_s)} \Leftrightarrow q(r_s) = \frac{m}{n}$$

where

$$q(r) = \frac{rB_{z0}(r)k}{B_{\theta0}(r)}$$

is called the safety factor (you can find a typical q profile in figure 3). In a torus, it gives the ratio of the times a magnetic field line travels around the torus “the long way” (toroidally) to “the short way” (poloidally). In the cylindrical tokamak, it gives the length in z (normalized by $2\pi R$) that is travelled by a magnetic field line during one twist in the circumferential direction.

3.1 Ideal Stability

3.1.1 Preliminary results

We can easily understand why a (m, n) instability will occur in the vicinity of r_s . In ideal MHD (we will suppose $\eta = 0$ in this section), the restoring force is the “tension” in the magnetic field lines that tries to prevent them to bend. We can easily see that if the perturbation of the magnetic field is not constant along the equilibrium magnetic field, this will cause the magnetic field lines to bend and there will be a restoring force. But if the perturbation is constant, then the field line is “translated” and there is no bending and thus no restoring force. The perturbation field will thus be singular at r_s . This “translation” gives this instability its name, the “interchange” instability because when the field lines are translated, it seems like they interchange place.

In order to quantify this “tension” in the magnetic field lines, let us go back to the equation of motion

$$\rho \frac{D\vec{v}}{Dt} = -\nabla p + (\nabla \times \vec{B}) \times \vec{B}$$

and, using vector calculus, rewrite it as

$$\rho \frac{D\vec{v}}{Dt} = -\nabla \left(p + \frac{\vec{B}^2}{2} \right) + \vec{B} \cdot \nabla \vec{B}$$

We have decomposed the magnetic force into a magnetic pressure $\vec{B}^2/2$ and a tension in field lines $\vec{B} \cdot \nabla \vec{B}$. Now we linearize this equation around the equilibrium and rewrite it in function of the

lagrangian displacement. We obtain by doing so equation 5 rewritten by using vector calculus identities

$$\rho\gamma^2\vec{\xi} = -\nabla(\vec{B}_0 \cdot \vec{B}_1) + \vec{B}_0 \cdot \nabla\vec{B}_1 + \vec{B}_1 \cdot \nabla\vec{B}_0 - \nabla p_1 \quad (8)$$

As we will show later on, in ideal MHD, the magnetic flux is frozen into the fluid and thus the fluid follows the bending of field lines. This motivates us to try the following ansatz for the perturbation fields : $\vec{B}_1 = b_r\hat{r}$, $\vec{\xi} = \xi_r\hat{r}$. This corresponds to a stretching of the magnetic field lines perpendicular to the magnetic surface. By injecting this into equations 8 and 6 and projecting on \hat{r} we get

$$\begin{aligned} \rho_0\gamma^2\xi_r &= \left(\frac{B_{\theta 0}im}{r} - B_{z0}ink \right) b_r - \frac{dp_1}{dr} \\ b_r &= \left(\frac{B_{\theta 0}im}{r} - B_{z0}ink \right) \xi_r \end{aligned}$$

where we have used $\vec{B}_0 \cdot \vec{B}_1 = 0$, $\partial_\theta = im/r$, $\partial_z = -ink$ and $B_{r0} = 0$. We finally obtain

$$\rho_0\gamma^2\xi_r = \left(\frac{B_{\theta 0}im}{r} - B_{z0}ink \right)^2 \xi_r - \frac{dp_1}{dr} = - \left(\frac{B_{\theta 0}n}{r} \right)^2 \left(\frac{m}{n} - q \right)^2 \xi_r - \frac{dp_1}{dr} \quad (9)$$

where we can clearly see that the restoring force vanishes for r_s such as $q(r_s) = m/n$. The instability will thus appear in the vicinity of r_s , and will be driven by the pressure appearing in the second term ($-\partial_r p_1$).

If we suppose $p_1 = 0$ and $q \neq m/n$, we get a wave equation with a frequency given by

$$\gamma = i \left(\frac{B_{\theta 0}im}{r} - B_{z0}ink \right) \equiv i\omega$$

This is no other than the shear Alfvén wave, the magnetic analogue to waves propagating on an ordinary string under tension. If we define $\vec{k} = \nabla(m\theta - nkz)$, we have for the group velocity

$$\vec{v}_g = \nabla_{\vec{k}}\omega = v_A\hat{B}_0 \text{ with } v_A = \frac{\|\vec{B}_0\|}{\sqrt{\rho_0}} \text{ and } \hat{B}_0 = \frac{\vec{B}_0}{\|\vec{B}_0\|}$$

As a reminder, the vacuum permeability μ_0 is one in our units system and the Alfvén velocity becomes thus in SI units $v_A = \|\vec{B}_0\|/\sqrt{\rho_0\mu_0}$. If we allow for compressible motion, we get the fast and slow magnetosonic waves. Their phase velocity is given in figure 8.

In ideal MHD, the magnetic flux is “frozen” into the fluid and thus in order to “break” field lines, resistivity is needed to allow for some diffusion of the magnetic field (you can find a demonstration of this result in the appendix “Frozen in theorem”). This means that ideal MHD does not allow any change in topology of the magnetic field lines, because they cannot break and reconnect. We can relax this constraint by adding some resistivity that adds the laplacian term in equation 2 which is typical of the diffusion process. We can measure the impact of resistivity on this equation by making it dimensionless :

$$\begin{aligned} \frac{B}{t_A} \frac{\partial \hat{B}}{\partial \hat{t}} &= \frac{Bv_A}{a} \hat{\nabla} \times (\hat{v} \times \hat{B}) + \frac{B}{a^2} \eta \hat{\Delta} \hat{B} \\ \frac{\partial \hat{B}}{\partial \hat{t}} &= \hat{\nabla} \times (\hat{v} \times \hat{B}) + \frac{1}{S} \hat{\Delta} \hat{B} \\ S &= \frac{t_R}{t_A} = \frac{\frac{a^2}{\eta}}{\frac{a}{v_A}} = \frac{av_A}{\eta} \end{aligned}$$

with a the minor radius, $t_A = a/v_A$ the Alfvén time, t_R the resistive time and S the Lundquist number i.e. the ratio of the resistive time t_R , time scale of the resistive diffusion processes, over the Alfvén time t_A . In modern fusion experiments, this number is typically in the range $S \sim 10^6 - 10^{12}$ [6]. In our units system, the Alfvén velocity, the Alfvén time and the minor radius are unity, and thus we have $S = \eta^{-1}$.

Ideal instabilities will have growth rates of order $1/t_A$ while resistive instabilities will have much lower growth rates of order $1/t_R$. This is the reason why the first step to assess the stability of a plasma configuration consists in computing its ideal MHD stability. If it is ideally unstable, adding resistivity makes almost no difference because S is high. If it is ideally stable, then adding resistivity can create new instabilities called resistive instabilities which are the subject of the present work.

3.1.2 Stability condition

We have now reached the limits of the assumption $\vec{B}_1 = b_r \hat{r}$, $\vec{\xi} = \xi_r \hat{r}$ and we will have to treat perturbations in full generality to obtain stability limits on the pressure, which we have identified as the driving force. As explained before, for $\eta = 0$, equation 6 turns into an algebraic equation, which allows us to eliminate \vec{B}_1 as a function of the displacement $\vec{\xi}$. We can eliminate p_1 thanks to equation 7 and recast the system 5 - 7 as

$$\rho_0 \frac{\partial^2 \vec{\xi}}{\partial t^2} = \vec{F}(\vec{\xi}) \quad (10)$$

where we have introduced the ideal MHD linear force operator, given by [6]

$$\vec{F}(\vec{\xi}) = (\nabla \times \vec{B}_0) \times (\nabla \times (\vec{\xi} \times \vec{B}_0)) + (\nabla \times (\nabla \times (\vec{\xi} \times \vec{B}_0))) \times \vec{B}_0 + \nabla(\vec{\xi} \cdot \nabla p_0 + \Gamma p_0 \nabla \cdot \vec{\xi})$$

Let us define a change in potential energy due to a perturbation

$$\delta W(\vec{\xi}^*, \vec{\xi}) = -\frac{1}{2} \int dV \vec{\xi}^* \cdot \vec{F}(\vec{\xi})$$

where the integration is over the entire plasma volume.

The self-adjointness of $\vec{F}(\vec{\xi})$, which can be shown by explicit calculation, allows us to use the energy principle that states that there is an instability if, and only if, there exists a vector field $\vec{\xi}$ that satisfies the boundary conditions, and such that [6]

$$\delta W(\vec{\xi}^*, \vec{\xi}) < 0$$

To prove instability, it is sufficient to find a test field for which δW is negative. To prove stability, we have to show that the minimum of δW over all permitted perturbation fields is positive. In order to find the field for which this minimum occurs, there are two possibilities. We can either (1) use the Euler-Lagrange equation on δW or (2) solve equation 10 with $\partial_{t^2} = 0$, i.e. $\vec{F}(\vec{\xi}) = 0$. We can indeed see from the definition of δW and the self-adjointness of $\vec{F}(\vec{\xi})$ that

$$\vec{F}(\vec{\xi}_c) = \vec{F}(\vec{\xi}_c^*) = 0 \Leftrightarrow \delta W \text{ is stationary at } \vec{\xi}_c$$

The second option is equivalent to solve for the mode with marginal stability ($\gamma = 0$).

If we choose the first case, following Newcomb [11], we can eliminate ξ_θ and ξ_z to get δW on $\xi \equiv \xi_r$ only

$$\delta W = \int_0^a dr \left(f \left(\frac{d\xi}{dr} \right)^2 + g \xi^2 \right) \quad (11)$$

The Euler-Lagrange equation then reads

$$\boxed{\frac{d}{dr} \left(f \frac{d\xi}{dr} \right) - g\xi = 0} \quad (12)$$

with f and g functions of equilibrium profiles only :

$$f(r) = \frac{rB_{\theta 0}^2(m-nq)^2}{n^2k^2r^2 + m^2}$$

$$g(r) = \frac{2n^2k^2r^2}{n^2k^2r^2 + m^2} \frac{dp_0}{dr} + \frac{B_{\theta 0}^2}{r}(m-nq)^2 \frac{n^2k^2r^2 + m^2 - 1}{n^2k^2r^2 + m^2} + \frac{2n^2k^2rB_{\theta 0}^2}{(n^2k^2r^2 + m^2)^2}(n^2q^2 - m^2)$$

The equation 12 is singular wherever $f(r)$ vanishes, i.e. at $r = 0$ and at r_s if $q(r_s) = \frac{m}{n}$ has a solution. The magnetic surface at r_s is called the singular surface for the parameters m and n considered. Note that m and n can be any natural number and thus there exists a singular surface at every radius for which $q(r)$ is rational. For the equilibrium profiles chosen, $q(r)$ is monotonically increasing and thus there exists up to one singular surface for each (m, n) couple.

From the definition of g , we can see that a negative radial pressure gradient is always destabilizing. This is the driving force of the interchange instability.

Following Newcomb[11][6], we define the local coordinate $x = |r - r_s|$ and expand f and g in a Taylor series in x (the prime denotes a radial derivative and h.o.t. stands for higher order terms)

$$f(x) = \sum_{n=0}^{\infty} f_n x^n = \frac{r_s B_{\theta 0}^2(r_s)(-nq'(r_s)x)^2}{n^2k^2r_s^2 + m^2} + \text{h.o.t.} = f_2 x^2 + \text{h.o.t.}$$

$$g(x) = \sum_{n=0}^{\infty} g_n x^n = \frac{2n^2k^2r_s^2}{n^2k^2r_s^2 + m^2} \frac{dp_0}{dr}(r_s) + \text{h.o.t.} = g_0 + \text{h.o.t.}$$

Using the definition of q , we can rewrite f_2 and g_0 as

$$f_2 = \frac{r_s B_{\theta 0}^2 B_{z0}^2}{B_0^2} \left(\frac{q'}{q} \right)^2$$

$$g_0 = \frac{2B_{\theta 0}^2}{B_0^2} \frac{dp_0}{dr}$$

where all the quantities are evaluated at r_s . We have of course $f_n = f^{(n)}/n!$ and the same for g .

As a reminder, a singular point x_0 of a homogeneous linear equation

$$y^n(x) + p_{n-1}(x)y^{n-1}(x) + \dots + p_1(x)y^1(x) + p_0(x)y(x) = 0$$

is regular if not all of $p_i(x)$ are analytic but if all of $(x - x_0)^{n-i}p_i(x)$ are analytic in a neighborhood of x_0 . If we rewrite equation 12 as

$$\xi'' + \frac{f'}{f}\xi' - \frac{g}{f}\xi = 0$$

and we inject $f = f_2 x^2$ and $g = g_0$, it appears clearly that $p_1 \sim x^{-1}$ and $p_0 \sim x^{-2}$, and thus that r_s is a regular singular point. This allows us to look for a solution under the form of a Frobenius expansion[12] in the vicinity of r_s :

$$\xi = |x|^\sigma \sum_{n=0}^{\infty} \xi_n x^n \quad (13)$$

By injecting the Frobenius expansion and the Taylor expansions of f and g into equation 12 and by equating the coefficients of each power of x to zero, we obtain two solutions for σ and the ξ_n , under the form of a recurrence relation :

$$\sigma_{\pm} = -\frac{1}{2} \pm \sqrt{\frac{1}{4} + \frac{g_0}{f_2}}$$

$$\xi_{n\pm} = \frac{-\sum_{j=0}^{n-1} \xi_{j\pm} (f_{n+2-j}(\sigma_{\pm} + j)(\sigma_{\pm} + n + 1) - g_{n-j})}{f_2(\sigma_{\pm} + n)(\sigma_{\pm} + n + 1) - g_0}$$

$$\xi_{\pm} = |x|^{\sigma_{\pm}} \sum_{n=0}^{\infty} \xi_{n\pm} x^n$$

Both σ_+ and σ_- are negative because f_2 is positive and g_0 is negative (the pressure is monotonically decreasing with r). The two solutions are thus singular at r_s as expected. The condition for σ_+ and σ_- to be real and unequal is

$$\frac{g_0}{f_2} > -\frac{1}{4}$$

which can be restated as a limit on the pressure gradient called Suydam's condition

$$-\frac{dp_0}{dr} < \frac{rB_{z0}^2}{8} \left(\frac{q'}{q}\right)^2$$

This condition will be shown to be necessary for stability. As predicted, the pressure gradient is the driving force of the instability. We can also understand why a high value of q' is stabilizing. The radial derivative of q , called the magnetic shear, gives basically the variation of the pitch angle of the equilibrium magnetic field lines with r . Now, we know that at r_s , it is the fact that this pitch angle is equal to the one of the lines on which the perturbations are constant that creates the instability by removing the restoring force associated with magnetic field line bending. If the magnetic shear is higher, the pitch angle of the equilibrium magnetic field lines will thus get far from its resonant value on r_s more quickly when r goes away from r_s .

Since we have two linearly independent solutions of a second order ODE, any solution can be written as a sum of these two. The solution with σ_+ (ξ_+) is called the “small” solution and the solution with σ_- (ξ_-) is called the “large” solution. These names come from their behaviour at the rational surface ($x \rightarrow 0$) and the fact that $\sigma_{\pm} < 0$ and $|\sigma_+| < |\sigma_-|$. Since equation 12 is homogeneous, each solution is defined up to an arbitrary multiplicative constant, and thus $\xi_{0\pm}$ is arbitrary and can be normalized to one.

The boundary condition at the edge comes from the fact that no plasma can flow into the wall ($\xi(1) = 0$). The boundary condition at $r = 0$ needs a bit more work. In order to expand f and g in a Taylor expansion from $r = 0$, we need to obtain the behaviour of $B_{\theta 0}$, B_{z0} , q and p_0 for small r . The task is easy for $B_{\theta 0}$ and p_0 because these are input equilibrium profiles for which we have a simple analytic form

$$p_0 = \hat{p}(1 - r^2) \simeq \hat{p}$$

$$B_{\theta 0}(r) = \hat{B}_{\theta} \frac{\frac{r}{r_0}}{1 + \left(\frac{r}{r_0}\right)^2} \simeq \hat{B}_{\theta} \frac{r}{r_0}$$

. Using the equilibrium equation at $r = 0$ we find for the two other profiles

$$\frac{d}{dr} \frac{1}{2} B_{z0}^2 = -\frac{dp_0}{dr} - \frac{B_{\theta 0}}{r} \frac{d}{dr} r B_{\theta 0} \Rightarrow \frac{dB_{z0}}{dr}(0) = 0 \Rightarrow B_{z0} \simeq B_{z0}(0)$$

$$q = \frac{rB_{z0}k}{B_{\theta 0}} \simeq q(0)$$

Thanks to these approximations we can rewrite f and g as $f \simeq \alpha r^3$ and $g \simeq \beta r$. We inject these expressions into equation 12

$$\frac{d}{dr} \left(\alpha r^3 \frac{d\xi}{dr} \right) - \beta r \xi = 0$$

and look for a power law solution $\xi = r^\sigma$. We find

$$\sigma = -1 \pm \sqrt{1 + \frac{\beta}{\alpha}} = -1 \pm m$$

In the present work we are only interested in the case $m > 1$ because we stick to equilibrium profiles for which $q(0)$ is larger than one and is monotonically increasing with r . It is therefore not possible to have a singular surface with $m = 1$ since $q(r_s) = m/n$ has in this case no solution. The solution with σ_+ is thus regular at the origin and is the physical solution while the one with σ_- is singular. We can conclude that ξ behaves like r^{m-1} for r going to zero.

As stated earlier, we are interested in the minimum value of $\delta W(\xi)$ over all the displacement fields compatible with the boundary conditions. We know that this minimum occurs for the displacement fields which are solutions of equation 12. Newcomb[11] has shown that the value of this minimum is positive (or equivalently, that the system is stable for the given (m,n) instability) if, and only if, (1) Suydam's condition is fulfilled at r_s , (2) the solution of equation 12 that is zero at $r = 0$ does not vanish in the interval $]0, r_s[$ and (3) the small solution of equation 12 (ξ_+) does not vanish in the interval $]r_s, 1[$.

We have now a straightforward method to assess the ideal stability of an axisymmetric flow-less equilibrium towards a helical (m,n) eigenmode in a cylindrical tokamak .

First compute the equilibrium profiles, locate the singular surface with $q(r_s) = m/n$, and check Suydam's condition.

Second integrate numerically equation 12 from $r = 0 + \epsilon_0$ to $r = r_s - \epsilon_l$ with the initial condition $\xi(\epsilon_0) = C\epsilon_0^{m-1}$ and $\xi'(\epsilon_0) = C(m-1)\epsilon_0^{m-2}$. The constant C is arbitrary due to the homogeneous nature of equation 12. We cannot start the integration at $r = 0$ because the ODE is singular there, so we start at a small distance ϵ_0 and we use the r^{m-1} behaviour shown before to find the initial conditions.

Third get the small solution by numerical integration from $r = r_s + \epsilon_r$ to $r = 1$ with the initial condition $\xi(r_s + \epsilon_r) = \xi_+(x = \epsilon_r)$ and $\xi'(r_s + \epsilon_r) = \xi'_+(x = \epsilon_r)$. The values of ξ_+ and ξ'_+ are obtained by computing the coefficients ξ_{n+} of the Frobenius expansion up to a certain n thanks to the recurrence relation. Due to the deterioration of accuracy in the numerical computation of higher order derivatives of f and g , we truncate to a low order ($n=3$) but choose a ϵ_r low enough to still have convergence of the serie. Check if the integrated solution does not vanish in the interval $]r_s, 1[$.

I implemented this method in Fortran. The ODE integration was performed with the help of a routine from the NAG library using the Backward Differentiation Formulae[17]. This implementation was used in my code to check ideal stability before starting the resistive stability study, which is our primary goal. Resistive effects are indeed of little importance when the system is ideally unstable since the resistive time scale is much longer than the Alfvén time scale, as explained before.

3.2 Resistive Stability - Asymptotic Matching

When the system is shown to be ideally stable, it can become unstable when resistivity is added to the model. In this case, resistivity is important only in a thin layer at the singular surface called the

resistive layer. The asymptotic matching method takes advantage of this property by separating the domain into 2 regions : an “inner” resistive layer at r_s which is thin enough so that the variation of the equilibrium quantities can be neglected and an “outer” region which takes the rest of the domain and where resistivity and inertia can be neglected. The idea of this method asymptotic matching method comes from several references, namely [2][16].

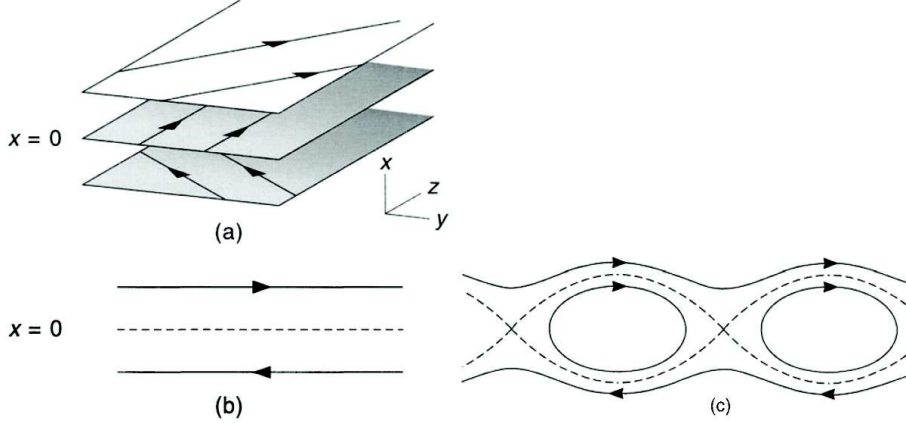


Figure 4: (a) Sheared slab model of magnetic reconnection. The lines are magnetic field lines. We can see this as a slab approximation of our system, with $x = r - r_s$. The planes are equivalent to the cylindrical magnetic surfaces, and the $x = 0$ plane is equivalent to the singular surface if we take \hat{z} as the direction of \vec{B}_0 at r_s and \hat{y} as $\vec{B}_0 \times \hat{r}$. Then we have $\vec{k} \equiv \nabla(m\theta - nkz)$ in the y direction. (b) Projection of the equilibrium field lines on the x, y plane. (c) Projection of the perturbed field lines on the x, y plane. [1]

3.2.1 Outer Region

Inertia and resistivity can be neglected in the outer region. We look thus for the marginally stable solutions of the linear ideal MHD equations. This means that we solve the system of equations 5 - 7 without the term $\rho_0 \gamma^2 \vec{\xi}$ in the first equation and the term $\frac{\eta}{\gamma} \nabla \times (\nabla \times \vec{B}_1)$ in the second one, i.e. we solve equation 12 again

$$\frac{d}{dr} \left(f \frac{d\xi}{dr} \right) - g\xi = 0$$

In order to neglect the term $\frac{\eta}{\gamma} \nabla \times (\nabla \times \vec{B}_1)$ for vanishing resistivity, we make the assumption that γ scales like a fractional power of η . This assumption can be shown to be consistent in figure 7 where the growth rate calculated with this method is given in function of the resistivity. In order to neglect the inertia term, we use the fact that the time scale on which the instability will grow will be of the order of the resistive time, which is higher than the Alfvén time by a factor of the Lundquist number ($S \sim 10^6 - 10^{12}$).

We know that the solutions of equation 12 are singular and thus not physical at r_s . By adding resistivity and inertia in the inner layer around r_s , we get a local solution that can match the two singular ideal solutions on both sides of the singular surface, giving a global physical solution for the displacement field strictly valid in the limit of vanishing resistivity.

Note that if we wanted to get the growth rate and the eigenfunction of the ideal interchange instability treated in the last section, we would have resolved the singularity of ξ at r_s by solving an inner region equation as well, but only with inertia and not resistivity.

This brings us to the new driving force that appears when resistivity is added : the equilibrium toroidal current gradient, or equivalently the magnetic shear. Contrarily to the pressure gradient for which the only values that matter are the one in the vicinity of the singular surface, for the current gradient it is spread into the whole domain. Still, resistivity is needed only in the inner region to permit the *reconnection* of the magnetic field that is resonant at r_s for the same reason as for the interchange mode, because the Alfen wave line bending stabilizing term vanishes for $\vec{k} \cdot \vec{B}_0 = 0$. In other words, the magnetic field is perturbed following ideal MHD in an extended region on both sides of the singular surface, and resistivity is needed in the inner region to break and reconnect field lines coming from both sides. Modes for which the current gradient is the main driving force are called *tearing modes*. The driving force coming from the pressure gradient is always present and the modes for which it is the main driving force are called *resistive interchange modes*.

We can get a physical picture of how resistivity creates reconnection in a sheared magnetic configuration in figure 4. As we can see in this figure, the reconnection open magnetic islands in which the magnetic field has a radial component, allowing for high heat transfer along these lines and thus creating a loss of confinement in the tokamak device.

Let us now describe the method of resolution in generality for a mode where both driving forces are present. A sketch of this method can be found in figure 5. First we compute ξ_l , the solution in the left outer region by numerically integrating from $r = 0 + \epsilon_0$ to $r = r_s - \epsilon_l$ with the initial condition $\xi_l(\epsilon_0) = C_l \epsilon_0^{m-1}$ and $\xi_l'(\epsilon_0) = C_l(m-1)\epsilon_0^{m-2}$ as we did in the second step of the aforementioned ideal stability method. The constant C is arbitrary due to the homogeneous nature of the ODE.

Second we compute ξ_r , the solution in the right outer region by numerically integrating from $r = 1$ to $r = r_s + \epsilon_r$. The initial condition at $r = 1$ is $\xi_r(1) = 0$ and $\xi_r'(1) = C_r$ with C_r arbitrary because of the homogeneous nature of the ODE. Notice that this time we compute the physical solution of equation 12 in the right region (i.e. the one that satisfies $\xi(1) = 0$) while the solution integrated in the third step of the aforementioned ideal stability method was the small solution ξ_- which does not satisfy the boundary condition at $r = 1$.

In order to perform the matching, we want a quantity that is independent of the arbitrary multiplicative constants. We know that the solutions ξ_l and ξ_r can be written as a sum of the small and large solutions

$$\begin{aligned}\xi_l &= c_{-l}\xi_- + c_{+l}\xi_+ = c_{-l}(\xi_- + \Delta_l\xi_+) \\ \xi_r &= c_{-r}\xi_- + c_{+r}\xi_+ = c_{-r}(\xi_- + \Delta_r\xi_+)\end{aligned}$$

where Δ_l and Δ_r are the ratios of coefficients of the small to the large solution and will be used as the matching parameters. The numerical integration from both sides gives us $\xi_l(r_s - \epsilon_l)$, $\xi_l'(r_s - \epsilon_l)$, $\xi_r(r_s + \epsilon_r)$ and $\xi_r'(r_s + \epsilon_r)$. We can compute $\xi_+(r_s - \epsilon_l)$, $\xi_+'(r_s - \epsilon_l)$, $\xi_-(r_s - \epsilon_l)$ and $\xi_-'(r_s - \epsilon_l)$ thanks to the recurrence relation giving the coefficients of the Frobenius expansion of the small and large solutions. If we define z_l as the ratio of ξ_l over its derivative, both obtained by numerical integration, we can write

$$z_l \equiv \frac{\xi_l(r_s - \epsilon_l)}{\xi_l'(r_s - \epsilon_l)} = \frac{c_{-l}(\xi_-(r_s - \epsilon_l) + \Delta_l\xi_+(r_s - \epsilon_l))}{c_{-l}(\xi_-'(r_s - \epsilon_l) + \Delta_l\xi_+'(r_s - \epsilon_l))}$$

We can isolate Δ_l to find

$$\Delta_l = \frac{z_l\xi_-'(r_s - \epsilon_l) - \xi_-(r_s - \epsilon_l)}{\xi_+(r_s - \epsilon_l) - z_l\xi_+'(r_s - \epsilon_l)}$$

The formulae for z_r and Δ_r are defined the same way.

A useful quantity is

$$\Delta' \equiv \Delta_l + \Delta_r$$

This is the conventional Δ' used in several papers[14][15] discussing resistive stability of pressureless equilibria. Indeed, when $p_0 = 0$ everywhere, the configuration is stable to all resistive modes

if $\Delta' < 0$ and unstable to tearing modes if $\Delta' > 0$. But when pressure is added, all configurations become unstable, and Δ' only gives a measure of the driving force coming from the current gradient.

To get the physical meaning of Δ' , we can go back to the potential energy change associated with the radial displacement $W(\xi)$ given in equation 11 and rewrite it in function of the radial magnetic field perturbation $\psi \equiv -iB_{1r} = B_{\theta 0}n(m/n - q)\xi/r$

$$\delta W(\psi) = \int_0^a dr \left(H \left(\frac{d\psi}{dr} \right)^2 + \left(\frac{g}{F^2} + \frac{1}{F} \frac{d}{dr} \left(H \frac{dF}{dr} \right) \right) \psi^2 \right)$$

with the associated Euler-Lagrange equation

$$\frac{d}{dr} \left(H \frac{d\psi}{dr} \right) - \left(\frac{g}{F^2} + \frac{1}{F} \frac{d}{dr} \left(H \frac{dF}{dr} \right) \right) \psi = 0$$

where $F(r) = \vec{k} \cdot \vec{B} = nkB_{z0} + m/rB_{\theta 0}$, $H(r) = r^3/(n^2k^2r^2 + m^2)$ and $g(r)$ was already defined. The integral should be understood as

$$\int_0^a = \int_0^{r_s - \epsilon} + \int_{r_s + \epsilon}^a$$

If we insert the Euler-Lagrange equation into the potential energy integral, we recognize the integrand as a derivative

$$\delta W_{\min}(\psi) = \int_0^a \frac{d}{dr} \left(H \psi \frac{d\psi}{dr} \right) = \left[H \psi \frac{d\psi}{dr} \right]_0^{r_s - \epsilon} + \left[H \psi \frac{d\psi}{dr} \right]_{r_s + \epsilon}^a = -H(r_s) \psi^2(r_s) \Delta'$$

where $\Delta' = (\psi'(r_s + \epsilon) - \psi'(r_s - \epsilon))/\psi(r_s)$ and where we have supposed that ψ is continuous ($\psi(r_s - \epsilon) = \psi(r_s + \epsilon)$). Since we have a second order ODE on each side of the rational surface, and a homogeneous boundary condition on $r = 0$ and $r = a$, if we impose the continuity of ψ , we cannot impose the continuity of ψ' , and thus it makes a jump, quantified by Δ' . Since $H(r)$ is always positive, δW_{\min} and Δ' are of opposite signs, and thus a positive Δ' means unstable while a negative one means stable. It is simple algebra to show that this last definition of Δ' is equivalent to $\Delta_l + \Delta_r$.

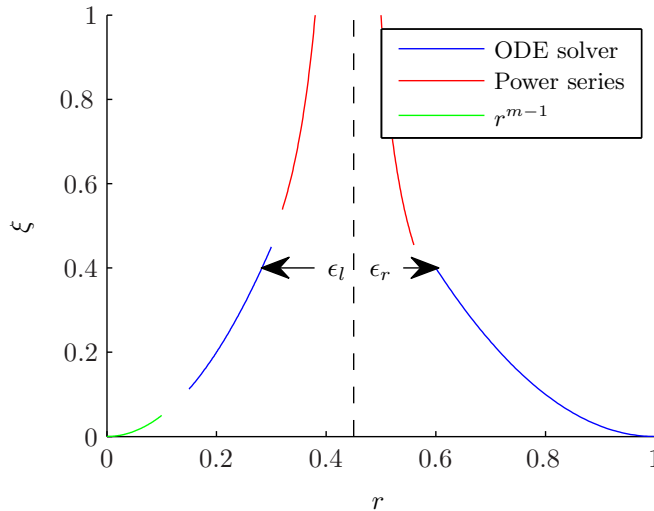


Figure 5: Sketch of the outer region solution for the radial displacement

3.2.2 Inner Region

In the inner region, resistivity and inertia must be taken into account, i.e. we solve the system of equations 5 - 7 without dropping any terms ($\gamma \neq 0$ and $\eta \neq 0$). On the other hand, this region is narrow enough so that the variation of the equilibrium quantities can be neglected. The system can be recast in the vicinity of r_s as[2][8]

$$\boxed{\frac{d^2}{dx^2} \Psi = U(x) \cdot \Psi} \quad (14)$$

with $x = \frac{r-r_s}{L_r}$ the scaled distance from the singular surface, $\Psi(x) = [\tilde{B}_{1r}(x), \xi(x), \tilde{B}_{1\parallel}(x)]$ a vector containing the scaled radial perturbed magnetic field, the radial displacement and the scaled perturbed magnetic field in the direction of the equilibrium magnetic field.

$$\begin{aligned} \tilde{B}_{1r}(x) &= \frac{ir_s}{nB_{\theta 0}q'L_r} B_{1r}(x) \\ \tilde{B}_{1\parallel}(x) &= \frac{-2B_0k^2}{q'^2B_{\theta 0}^2} B_{1\parallel}(x) \\ B_{1\parallel} &= \frac{\vec{B}_1 \cdot \vec{B}_0}{\|\vec{B}_0\|} \end{aligned}$$

The length scale L_r that appears in the derivation of equation 14 from the system 5-7 is given by

$$L_r = \left(\frac{\rho_0 \eta^2 r_s^2}{n^2 B_{\theta 0}^2 q'^2} \right)^{\frac{1}{6}}$$

where all quantities are evaluated at r_s . The coefficients are given by

$$U = \begin{pmatrix} Q & -xQ & 0 \\ -x/Q & x^2/Q & -(E+F)/Q^2 \\ -x/Q & -(G-E/F)Q & x^2/Q + (G+1)Q \end{pmatrix}$$

where $Q = \gamma/Q_r$ is the scaled growth rate and E, F and G, first defined in Ref. [8], are constants characterizing the equilibrium at r_s which can be written in our case as

$$\begin{aligned} E + F &= \frac{-2\rho_0' r_s k^2}{B_{\theta 0}^2 q'^2} \\ F &= \frac{\rho_0'^2 r_s^2 k^2}{B_{\theta 0}^4 q'^2} \\ G &= \frac{1}{\Gamma} \frac{B_0^2}{\rho_0} \end{aligned}$$

where all the quantities are evaluated at r_s . The growth rate scale Q_r is easily found since in our units system in which μ_0 is unity, η is a diffusion coefficient and has thus the dimension of a length squared over time. We conclude

$$Q_r = \frac{\eta}{L_r^2} = n^{\frac{2}{3}} \frac{1}{t_R^{\frac{1}{3}} t_A^{\frac{2}{3}}}$$

where we have defined the appropriate Alfvén time $t_A = \frac{r_s \sqrt{\rho_0}}{B_\theta}$ and resistive time $t_R = (1/q')^2/\eta$. We take $1/q'$ as the length scale for the resistive time because the shear is the driving force for

reconnection. Note that, while in the ideal case the magnetic shear was stabilizing because the mode was off resonance more quickly when leaving $r = r_s$, it is now destabilizing because it drives the reconnection of magnetic field lines. The instability grows thus on a time scale which is hybrid between resistive and Alfvénic.

We are now interested in the asymptotic solution of the inner equation 14 for $|x| \rightarrow \infty$. The inner solution for $x \rightarrow \infty$ will be matched with the outer solution for $r \rightarrow r_s^+$ and the inner solution for $x \rightarrow -\infty$ will be matched with the outer solution for $r \rightarrow r_s^-$.

Actually we need only to solve the inner equation for $x > 0$ thanks to a certain parity conserving property of this equation. Even solutions for $\Psi_1 = \tilde{B}_{1r}(x)$ couple only to odd solutions for $\Psi_2 = \xi(x)$ and $\Psi_3 = \tilde{B}_{1\parallel}(x)$ and vice versa[16]. A demonstration is given in the appendix ‘‘Parity conservation’’. This allows us to look for definite parity modes and gives us corresponding boundary conditions[16], i.e. for odd modes

$$\Psi'_1(0) = \Psi_2(0) = \Psi_3(0) = 0 \quad (15)$$

and for even modes

$$\Psi_1(0) = \Psi'_2(0) = \Psi'_3(0) = 0 \quad (16)$$

The parity of the mode is thus defined following the parity of the radial displacement $\Psi_2 \equiv \xi$.

Since the point at infinity is an irregular singular point of equation 14, we have to use a modified version of the Frobenius expansion we have introduced before : we allow now for an exponential ‘‘controlling factor’’ multiplying the power series[12]

$$\Psi = e^{S(x)} |x|^\sigma \begin{pmatrix} \sum_{n=-n_1}^{\infty} \psi_{n,1} \frac{1}{x^n} \\ \sum_{n=-n_2}^{\infty} \psi_{n,2} \frac{1}{x^n} \\ \sum_{n=-n_3}^{\infty} \psi_{n,3} \frac{1}{x^n} \end{pmatrix} \quad (17)$$

To find $S(x)$ we take the limit of U and keep only the dominant terms

$$\lim_{x \rightarrow +\infty} U(x) = \begin{pmatrix} 0 & 0 & 0 \\ 0 & x^2/Q & 0 \\ 0 & 0 & x^2/Q \end{pmatrix}$$

Since U is in this limit diagonal, we are left with 3 independent Schrödinger equations

$$\frac{d^2}{dx^2} \Psi_i(x) = \lambda_i(x) \Psi_i(x)$$

For $\lambda_1 = 0$, we have $\frac{d^2}{dx^2} \Psi_1(x) = 0$ and thus the solution for $\Psi_1(x)$ is a first degree polynomial that will be integrated in the power series part of the ansatz of equation 17. This means that there is no need for an exponential controlling factor for this eigenvalue, and thus $S_1(x) = 0$. For the two other ones, we inject the ansatz $\Psi(x) = e^{S(x)}$ (which is actually the WKB ansatz of quantum mechanics) and find

$$S''(x) + (S'(x))^2 = \frac{x^2}{Q}$$

Near an irregular singular point, it is usually true that[12]

$$S''(x) \ll (S'(x))^2$$

This assumption will be shown to be consistent afterwards. We finally obtain the Eikonal equation

$$(S'(x))^2 = \frac{x^2}{Q}$$

whose solution is

$$S(x) = C \pm \frac{x^2}{2\sqrt{Q}}$$

with C an arbitrary integration constant. We have thus three solutions for $S(x) : 0$ and $\pm \frac{x^2}{2\sqrt{Q}}$. We use each of them into equation 17 and inject the ansatz into equation 14. By equating the terms for each power of x , we find 2 solutions for σ and the coefficients ψ_n for each value of $S(x)$, i.e. 6 solutions in total

$$\begin{aligned}\Psi_{1\pm} &= |x|^{\sigma_{1\pm}} \begin{pmatrix} \sum_{n=-1}^{\infty} \psi_{n,1,1\pm} 1/x^n \\ \sum_{n=0}^{\infty} \psi_{n,2,1\pm} 1/x^n \\ \sum_{n=0}^{\infty} \psi_{n,3,1\pm} 1/x^n \end{pmatrix} \\ \Psi_{2\pm} &= \exp\left(\frac{x^2}{2\sqrt{Q}}\right) |x|^{\sigma_{2\pm}} \begin{pmatrix} \sum_{n=1}^{\infty} \psi_{n,1,2\pm} 1/x^n \\ \sum_{n=0}^{\infty} \psi_{n,2,2\pm} 1/x^n \\ \sum_{n=0}^{\infty} \psi_{n,3,2\pm} 1/x^n \end{pmatrix} \\ \Psi_{3\pm} &= \exp\left(-\frac{x^2}{2\sqrt{Q}}\right) |x|^{\sigma_{3\pm}} \begin{pmatrix} \sum_{n=1}^{\infty} \psi_{n,1,3\pm} 1/x^n \\ \sum_{n=0}^{\infty} \psi_{n,2,3\pm} 1/x^n \\ \sum_{n=0}^{\infty} \psi_{n,3,3\pm} 1/x^n \end{pmatrix}\end{aligned}$$

where the coefficients of the power series are given by a recurrence relation. The expressions of this relation and of $\sigma_{2\pm}$ and $\sigma_{3\pm}$ are too lengthy to appear here. The crucial part is that we find

$$\sigma_{1\pm} = -\frac{1}{2} \pm \sqrt{\frac{1}{4} - (E + F)} = -\frac{1}{2} \pm \sqrt{\frac{1}{4} + \frac{g_0}{f_2}} \equiv \sigma_{\pm}$$

where σ_{\pm} are the leading exponents of the previously defined large and small solutions of the outer equation in the vicinity of r_s . Since equation 14 is a system of three second order ODEs, any solution can be written as a linear combination of the six linearly independent solutions we have found

$$\Psi = \sum_{i=1\pm,2\pm,3\pm} \alpha_i \Psi_i$$

The requirement that the solution does not diverge exponentially at large x gives us $\alpha_{2\pm} = 0$. This means that at large x , the solution is dominated by $\Psi_{1\pm}$. Since the second component of Ψ , $\Psi_2 \equiv \xi$, is the radial displacement, the inner solution for ξ is for large x given by

$$\xi^{(i)} \sim \alpha_{1+} x^{\sigma_+} \left(1 + \xi_{1+}^{(i)} \frac{1}{x} + \xi_{2+}^{(i)} \frac{1}{x^2} + \dots\right) + \alpha_{1-} x^{\sigma_-} \left(1 + \xi_{1-}^{(i)} \frac{1}{x} + \xi_{2-}^{(i)} \frac{1}{x^2} + \dots\right)$$

where $\xi_{n\pm}^{(i)} \equiv \psi_{n,2,1\pm}$. We can show with the recurrence relation that the only non vanishing coefficients are even, and thus

$$\xi^{(i)} \sim \alpha_{1+} x^{\sigma_+} \left(1 + \xi_{2+}^{(i)} \frac{1}{x^2} + \xi_{4+}^{(i)} \frac{1}{x^4} + \dots\right) + \alpha_{1-} x^{\sigma_-} \left(1 + \xi_{2-}^{(i)} \frac{1}{x^2} + \xi_{4-}^{(i)} \frac{1}{x^4} + \dots\right) \equiv \alpha_{1+} \xi_+^{(i)} + \alpha_{1-} \xi_-^{(i)}$$

As a reminder, $x = (r - r_s)/L_r$ and the outer solution near r_s is given by

$$\begin{aligned}\xi^{(o)} &\sim c_+ |r - r_s|^{\sigma_+} \left(1 + \xi_{1+}^{(o)} (r - r_s) + \xi_{2+}^{(o)} (r - r_s)^2 + \dots\right) + c_- |r - r_s|^{\sigma_-} \left(1 + \xi_{1-}^{(o)} (r - r_s) + \xi_{2-}^{(o)} (r - r_s)^2 + \dots\right) \\ &\equiv c_+ \xi_+ + c_- \xi_-\end{aligned}$$

We can see that as long as the first term of the power series is concerned, we can identify $\xi_+^{(i)}$ as ξ_+ , the previously defined small solution, and $\xi_-^{(i)}$ as ξ_- , the large solution. The quantity of interest

to perform the matching is therefore $\Delta \equiv \frac{\alpha_{1+}}{\alpha_{1-}}$, the ratio of the coefficients of the small to the large solution.

In order to get this ratio, we need to integrate equation 14 from $x = 0$ where we have a boundary condition given by equation 15 if we solve for the odd mode, and by equation 16 for the even one. We integrate until a x large enough so that the small and large solutions are dominant and we can deduce the ratio from the value of the function and its derivative at that point. Various implementations of this computation are described in Ref. [16]. While I implemented the equilibrium and the outer region equation solvers from scratch, I used a routine that had already been written by the authors of Ref. [16] for this step. I only had to make minor changes to make it work. This routine took as input the equilibrium parameters E, F, G and the scaled growth rate Q and returned two ratios, one for the odd solution $\Delta_o(Q)$ and one for the even one $\Delta_e(Q)$. We have thus the odd inner solution $\xi_o = \xi_- + \Delta_o(Q)\xi_+$ and the even inner solution $\xi_e = \xi_- + \Delta_e(Q)\xi_+$.

3.2.3 Matching

To sum up, in the right region ($x > 0$), the outer solution is given by

$$\xi_r = c_r(\xi_- + \Delta_r \xi_+)$$

and the inner solution by

$$\xi_r^{(i)} = c_o \xi_o + c_e \xi_e = (c_o + c_e)\xi_- + (c_o \Delta_o(Q) + c_e \Delta_e(Q))\xi_+$$

If we want the coefficients of the small and large solutions to be continuous, we impose

$$c_r = c_o + c_e \tag{18}$$

$$c_r \Delta_r = c_o \Delta_o(Q) + c_e \Delta_e(Q) \tag{19}$$

In the left region ($x < 0$), the outer solution is given by

$$\xi_l = c_l(\xi_- + \Delta_l \xi_+)$$

and the inner solution by

$$\xi_l^{(i)} = c_o \xi_o - c_e \xi_e = (c_o - c_e)\xi_- + (c_o \Delta_o(Q) - c_e \Delta_e(Q))\xi_+$$

If we want the coefficients of the small and large solutions to be continuous, we impose

$$c_l = c_e - c_o \tag{20}$$

$$c_l \Delta_l = c_e \Delta_e(Q) - c_o \Delta_o(Q) \tag{21}$$

By injecting equation 18 into equation 19 and equation 20 into equation 21, we are left with a homogeneous system on c_o and c_e whose solubility condition is given by

$$D(Q) \equiv \begin{vmatrix} \Delta_r - \Delta_e(Q) & \Delta_r - \Delta_o(Q) \\ \Delta_l - \Delta_e(Q) & -(\Delta_l - \Delta_o(Q)) \end{vmatrix} = 0$$

By using the bisection method to find the root of $D(Q)$, we finally obtain the growth rate Q (the eigenvalue). Then we solve the system to find c_e, c_o, c_l and c_r and thus the spatial representation of the mode $\xi(r)$ (the eigenfunction).

Let us examine under what conditions this asymptotic matching method can give accurate results. As we have said earlier, only the first term of the power series of the large and small solutions match for inner and outer solutions :

$$\xi_{\pm}^{(i)}(x) = |x|^{\sigma_{\pm}} \left(1 + \xi_{2\pm}^{(i)} \frac{1}{x^2} + \dots \right)$$

$$\xi_{\pm}^{(o)}(x) = |x|^{\sigma_{\pm}} L_r^{\sigma_{\pm}} \left(1 + \xi_{1\pm}^{(o)} L_r x + \dots \right)$$

This means that the matching must be performed in a region in which we have

$$\xi_{2\pm}^{(i)} \frac{1}{x^2} \ll 1 \text{ and } \xi_{1\pm}^{(o)} L_r x \ll 1$$

This region is thus defined by

$$\sqrt{\xi_{2\pm}^{(i)}} \ll x \ll \frac{1}{\xi_{1\pm}^{(o)} L_r}$$

and exists only if

$$E_{\pm}(\eta) \equiv \sqrt{\xi_{2\pm}^{(i)}(\eta) \xi_{1\pm}^{(o)} L_r(\eta)} \ll 1$$

We emphasize the dependance of this criterion on η because it is the small parameter that allows us to use the asymptotic matching. We can see on figure 9 that E_- becomes of order one for a certain maximum η_c after which asymptotic matching cannot be used any more. This maximal resistivity gets lower with lower equilibrium pressure (β). We indeed had to choose a sufficiently high beta to find a resistivity interval in which we have accurate solutions coming from the asymptotic matching method and from the finite elements code M3DC1. We can also notice that the function E_- exhibits a local minimum while we would expect a monotonically increasing function of η . This behaviour has never been published to our knowledge. The small solution is not a concern since E_+ is always far below one for the range of resistivity considered.

There is another reason why a higher pressure makes the asymptotic matching method more accurate. This whole method is based on the decomposition of the solution into a large and a small solution whose leading terms near the singular surface are, respectively, $|x|^{\sigma_-}$ and $|x|^{\sigma_+}$ with

$$\sigma_{\pm} = -\frac{1}{2} \pm \sqrt{\frac{1}{4} - (E + F)} = -\frac{1}{2} \pm \sqrt{\frac{1}{4} + \frac{2p' r_s k^2}{B_{\theta}^2 q'^2}} \equiv -\frac{1}{2} \pm \frac{1}{2} \sqrt{1 - \alpha}$$

where all quantities are equilibrium profiles evaluated at the singular surface and where $\alpha \equiv \frac{p'}{p'_{Suydam}}$ is the ratio of the equilibrium pressure gradient at the rational surface on the maximal value for this gradient imposed by the aforementioned Suydam condition. As a reminder, the Suydam condition is a necessary condition for ideal stability. In order to study resistive stability we are thus interested in the range $]0, 1[$ for α . As the pressure increases, α goes to one, which makes the two exponents σ_{\pm} , and therefore the large and small function values, closer to each other. It is then more numerically accurate to separate two contributions that are of the same order than two contributions with one much larger than the other. More precisely, when we calculated the ratio $\Delta \equiv \frac{c_+}{c_-}$ of the coefficients of the small and large solutions in the outer region solution, for example on the right side of the singular surface, this was equivalent to solve the following linear system

$$\begin{pmatrix} \xi_+(r_s + \epsilon) & \xi_-(r_s + \epsilon) \\ \xi'_+(r_s + \epsilon) & \xi'_-(r_s + \epsilon) \end{pmatrix} \begin{pmatrix} c_+ \\ c_- \end{pmatrix} = \begin{pmatrix} \xi(r_s + \epsilon) \\ \xi'(r_s + \epsilon) \end{pmatrix} \Leftrightarrow Ax = b$$

where the elements of A are obtained from the Frobenius expansion and the elements of b are obtained from numerical integration from $r = 1$. If we inject in A the leading terms of the Frobenius expansions

$$A = \begin{pmatrix} \epsilon^{\sigma_+} & \epsilon^{\sigma_-} \\ \sigma_+ \epsilon^{\sigma_+ - 1} & \sigma_- \epsilon^{\sigma_- - 1} \end{pmatrix} \quad (22)$$

we can intuitively guess that this matrix will be better conditioned if σ_+ and σ_- are closer to each other, since it reduces the ratio of the diagonal terms. As a reminder, the condition number of a matrix A gives a bound on the error on x a small error on b can cause. The figure 10 shows indeed that the condition number of A is a decreasing function of α .

When the equilibrium pressure gradient vanishes at the rational surface ($\alpha = 0$), we have $\sigma_- = -1$ and $\sigma_+ = 0$, which means that the two Frobenius expansions

$$\xi_{\pm} = |x|^{\sigma_{\pm}} \sum_{n=0}^{\infty} \xi_{\pm n} x^n$$

are not linearly independent any more. In order to make it linearly independent, we have to modify ξ_- by adding a term of the form $x \log |x| \sum_{n=0}^{\infty} \xi_n x^n$ [12] [15]. The rest of the analysis is similar.

4 The M3DC1 code

The M3DC1 code implements a high-order implicit finite element method for integrating the time-dependent, linear and non linear, extended magnetohydrodynamic equations in two and three dimensions in an axisymmetric device [13]. While its extended capabilities make it useful for analyzing existing experimental data and for predicting operational limits of future devices, I used it to solve the aforementioned cylindrical tokamak test case for which we have an asymptotic matching solution. We can therefore benchmark the 2D linear resistive MHD capabilities of the M3DC1 code by comparing the results obtained for the growth rate of resistive modes with the ones computed with the asymptotic matching method. In order to get growth rates with M3DC1, I had to implement the equilibrium used in this study, generate meshes that are refined around the singular surface where a high spatial resolution is needed and perform a convergence study on the number of nodes and on the time step.

The following description of the code relies heavily on several papers [13][7][10].

4.1 Temporal discretization

We want an implicit temporal discretization so that we are not limited by the Courant–Friedrichs–Lewy condition associated with the fast and Alfvén waves. This is even more important for a resistive study because resistive instabilities grow on a much slower time scale than the Alfvén time.

Let us rewrite the linear resistive MHD equations (equations 1-3) as

$$\rho_0 \frac{\partial \vec{v}}{\partial t} = \vec{F}_1(\vec{B}, p) \quad (23)$$

$$\frac{\partial \vec{B}}{\partial t} = \vec{F}_2(\vec{v}) + \eta \Delta \vec{B} \quad (24)$$

$$\frac{\partial p}{\partial t} = F_3(\vec{v}) \quad (25)$$

where we have dropped the subscript one for the perturbation fields and where $\vec{F}_1, \vec{F}_2, F_3$ are linear differential operators.

We use the method of differential approximation which consists in evaluating the right terms of the last equations at a time $t^{n+1/2} = t^n + \theta\delta t$ with $\theta \in]0, 1]$ the implicitness parameter. First we find the velocity advance equation by using a Taylor expansion in time on \vec{B} and p

$$\rho_0 \frac{\partial \vec{v}}{\partial t} = \vec{F}_1(\vec{B}^{n+1/2}, p^{n+1/2}) = \vec{F}_1(\vec{B}^n + \frac{\partial \vec{B}}{\partial t} \theta \delta t, p^n + \frac{\partial p}{\partial t} \theta \delta t) \equiv \vec{F}_1(\tilde{\mathbf{B}}^n + \frac{\partial \tilde{\mathbf{B}}}{\partial t} \theta \delta t)$$

with $\tilde{\mathbf{B}} \equiv [\vec{B}, p]$. In order to get the time derivative of $\tilde{\mathbf{B}}$, we execute the same method on the two other equations and we neglect the resistive term $\eta \Delta \vec{B}$ (this term will be taken into account in the field advance equation)

$$\frac{\partial \tilde{\mathbf{B}}}{\partial t} = \tilde{\mathbf{F}}_{23}(\vec{v}^n + \frac{\partial \vec{v}}{\partial t} \theta \delta t)$$

with $\tilde{\mathbf{F}}_{23}(\vec{v}) = [\vec{F}_2(\vec{v}), F_3(\vec{v})]$. Now we inject this last relation, we use the linear property of the operators, and we discretize $\partial_t \vec{v}$ by $(\vec{v}^{n+1} - \vec{v}^n)/\delta t$ to finally get the velocity advance equation

$$(\rho_0 - \theta^2 \delta t^2 \vec{F}_1 \circ \tilde{\mathbf{F}}_{23}) \vec{v}^{n+1} = (\rho_0 + \theta(1 - \theta) \delta t^2 \vec{F}_1 \circ \tilde{\mathbf{F}}_{23}) \vec{v}^n + \delta t \vec{F}_1(\tilde{\mathbf{B}}^n)$$

Notice that $\vec{F}_1 \circ \tilde{\mathbf{F}}_{23}$ is no other than the aforementioned ideal MHD linear force operator $\vec{F}(\vec{\xi})$ since we find from equations 23-25 with $\eta = 0$ that

$$\partial_{t^2} \vec{\xi} = \vec{F}_1 \circ \tilde{\mathbf{F}}_{23}(\vec{\xi})$$

We can now implicitly advance the fields with the advanced velocity value

$$\frac{\partial \vec{B}}{\partial t} = \vec{F}_2(\vec{v}^{n+1/2}) + \eta \Delta \vec{B}^{n+1/2} = \delta t \theta (\vec{F}_2(\vec{v}^{n+1}) + \eta \Delta \vec{B}^{n+1}) + (1 - \theta) \delta t (\vec{F}_2(\vec{v}^n) + \eta \Delta \vec{B}^n)$$

We discretize $\partial_t \vec{B}$ by $(\vec{B}^{n+1} - \vec{B}^n)/\delta t$ and finally obtain

$$(1 - \delta t \eta \Delta) \vec{B}^{n+1} = \vec{B}^n + \delta t \theta \vec{F}_2(\vec{v}^{n+1}) + \delta t (1 - \theta) (\vec{F}_2(\vec{v}^n) + \eta \Delta \vec{B}^n)$$

Similarly, we find for the pressure

$$p^{n+1} = p^n + \delta t \theta F_3(\vec{v}^{n+1}) + \delta t (1 - \theta) F_3(\vec{v}^n)$$

This method can be shown to be stable for $\theta \geq 1/2$ and second-order time accurate for $\theta = 1/2$ [7]. A slightly modified version of this algorithm with better convergence properties called the Caramana method was used[7].

4.2 Spatial discretization

In 2D mode, an unstructured triangular mesh is generated on the cross section of the tokamak (which is in our case circular). The toroidal (axial in our case of the cylindrical tokamak) dependance of the perturbations is assumed to be e^{-inkz} as it was for the asymptotic matching method. In other words the axial derivative ∂_z is replaced by $-ink$ when applied to a perturbation field. On the other hand, there is no such assumption for the poloidal (circumferential) dependance this time since the equations are solved in full generality on the cross section.

Without loss of generality, the velocity and the magnetic field are expressed the following way[13]

$$\vec{v} = \nabla U \times \hat{z} + \nabla \chi + v_z \hat{z}$$

$$\vec{B} = \nabla\psi \times \hat{z} + B_z\hat{z} - \nabla_{\perp}(\partial_z f)$$

where $\nabla_{\perp} = \hat{x}\partial_x + \hat{y}\partial_y$ is the gradient in the plane. With this definition for \vec{B} , the divergence free nature of the axisymmetric equilibrium magnetic fields $\vec{B}_0(r)$ we treat is obvious : the divergence of the first term always vanishes, the divergence of the second term vanishes because B_{z0} does not depend on z and finally the third term vanishes because f_0 does not depend on z . By imposing the divergence of the perturbed magnetic field $\vec{B}_1(r, \theta)e^{-inkz}$ to vanish, we get an equation on B_z and f

$$\nabla \cdot \vec{B}_1 = \partial_z B_{z1} - \Delta_{\perp}(\partial_z f_1) = 0 \Rightarrow B_{z1} = \Delta_{\perp} f_1$$

where $\Delta_{\perp} = \nabla \cdot \nabla_{\perp}$ and where we have used $\partial_z = -ink$. Thanks to the last relation, we can keep only f as an independent scalar field and compute B_z from it when needed. With the pressure p , we have thus six independent scalar fields : ψ, f, U, χ, v_z and p .

On each triangular element, the scalar fields are expressed as a sum of 18 polynomial basis functions[13]

$$U(x, y, t^n) = \sum_{j=1}^{18} U_j^n \nu_j(x, y)$$

Again, we make no assumption at all on the spatial dependance of the fields in the plane, and thus we use 2D cartesian coordinates ($x = r \cos \theta, y = r \sin \theta$). On each node, there are six degrees of freedom for each scalar field, i.e. the function value, its two first derivatives (∂_x, ∂_y) and its three second derivatives ($\partial_{xx}, \partial_{yy}, \partial_{xy}$). Basis functions $\nu_j(x, y)$ are chosen that are piecewise quintic with the property that the function and its first derivative are continuous across element boundaries. Each basis function has the value 1 for one of the six degrees of freedom at one node, and has the value 0 for every other degree of freedom on every other node.

We inject these expressions for the velocity and the magnetic field into the time advance equations from the last section, we apply projection operators and we multiply by each basis function and integrate over the whole domain. Then we perform integration by parts to reduce the order of the differential operator applied to the scalar fields. The surface terms appearing from this depend on the boundary condition applied. Homogeneous Dirichlet or Neumann boundary conditions are

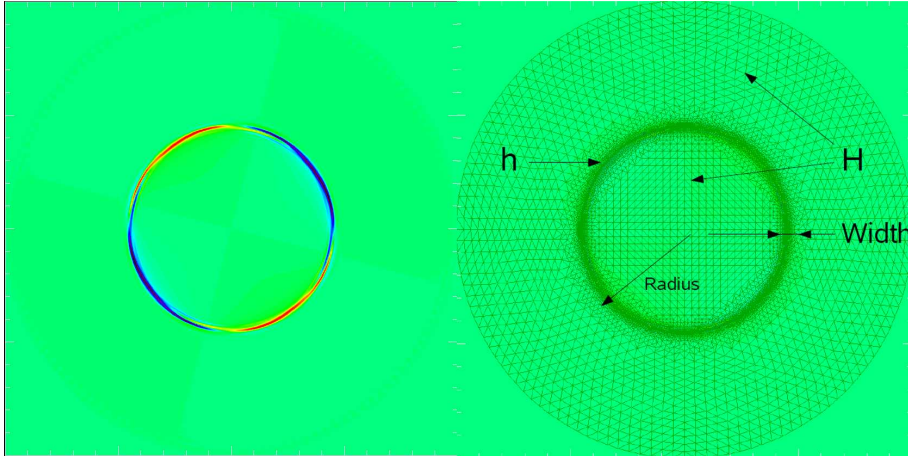


Figure 6: (Left) Radial velocity profile obtained with M3DC1 for a $m = 2, n = 1$ instability. Note that the $m = 2$ poloidal dependance appeared on its own and was not assumed anywhere in the code (Right) Mesh used for the simulation.

applied for a given scalar field by removing in its linear combination the basis functions that have, respectively, its values or the value of its normal derivatives that vanish at the border.

We end up with the following matricial equations. First the velocity advance

$$\begin{pmatrix} S_{11}^v & S_{12}^v & S_{13}^v \\ S_{21}^v & S_{22}^v & S_{23}^v \\ S_{31}^v & S_{32}^v & S_{33}^v \end{pmatrix} \begin{pmatrix} U \\ v_z \\ \chi \end{pmatrix}^{n+1} = \begin{pmatrix} D_{11}^v & D_{12}^v & D_{13}^v \\ D_{21}^v & D_{22}^v & D_{23}^v \\ D_{31}^v & D_{32}^v & D_{33}^v \end{pmatrix} \begin{pmatrix} U \\ v_z \\ \chi \end{pmatrix}^n + \begin{pmatrix} R_{11}^v & R_{12}^v & R_{13}^v \\ R_{21}^v & R_{22}^v & R_{23}^v \\ R_{31}^v & R_{32}^v & R_{33}^v \end{pmatrix} \begin{pmatrix} \psi \\ f \\ p \end{pmatrix}^n$$

where ψ , f , U , χ , v_z and p are $6M$ vectors (M is the number of nodes), each element being the coefficient of the corresponding basis function. The matrices S , D and R are $6M$ by $6M$. The field advance equation is given by

$$\begin{pmatrix} S_{11}^b & S_{12}^b \\ S_{21}^b & S_{22}^b \end{pmatrix} \begin{pmatrix} \psi \\ f \end{pmatrix}^{n+1} = \begin{pmatrix} D_{11}^b & D_{12}^b \\ D_{21}^b & D_{22}^b \end{pmatrix} \begin{pmatrix} \psi \\ f \end{pmatrix}^n + \begin{pmatrix} R_{11}^b & R_{12}^b & R_{13}^b \\ R_{21}^b & R_{22}^b & R_{23}^b \end{pmatrix} \begin{pmatrix} U \\ v_z \\ \chi \end{pmatrix}^{n+1} \\ + \begin{pmatrix} Q_{11}^b & Q_{12}^b & Q_{13}^b \\ Q_{21}^b & Q_{22}^b & Q_{23}^b \end{pmatrix} \begin{pmatrix} U \\ v_z \\ \chi \end{pmatrix}^n$$

The pressure advance equation is given by

$$S_{11}^p p^{n+1} = D_{11}^p p^n + \begin{pmatrix} R_{11}^p & R_{12}^p & R_{13}^p \end{pmatrix} \begin{pmatrix} U \\ v_z \\ \chi \end{pmatrix}^{n+1} + \begin{pmatrix} Q_{11}^p & Q_{12}^p & Q_{13}^p \end{pmatrix} \begin{pmatrix} U \\ v_z \\ \chi \end{pmatrix}^n$$

We can note that there exists two important simpler sub-systems[4][13]. The first one is obtained by setting v_z , χ , f and p to zero and by keeping only the first equation in the velocity advance and in the field advance. This is called the two-fields (U, ψ) reduced system. The second one is obtained by setting χ and p to zero and by keeping only the first two equations in the velocity advance and in the field advance. This is called the four-fields (U, ψ, f, v_z) reduced system. These are valuable for debugging and for better understanding of the different physical effects that appear when we allow for more fields[13].

We can take advantage of the fact that all matrices in the previous equations are constant in time. This means that at each time step, we solve systems of the type

$$\mathbf{A} \cdot \mathbf{x}^{n+1} = \mathbf{b}^n$$

with \mathbf{A} constant. If we decompose \mathbf{A} once for all into a lower diagonal and an upper diagonal form ($\mathbf{A} = \mathbf{L} \cdot \mathbf{U}$), i.e. if we perform a Gaussian elimination, then we only have to execute two back substitution at each time step. First we solve

$$\mathbf{L} \cdot \mathbf{y} = \mathbf{b}^n$$

for the vector \mathbf{y} by back substitution from the top and then we solve

$$\mathbf{U} \cdot \mathbf{x}^{n+1} = \mathbf{y}$$

for \mathbf{x}^{n+1} by back substitution from the bottom[6]. A package named SUPERLU[5] was used as a LU decomposer especially efficient on sparse matrices like ours.

4.3 Implementation of the cylindrical tokamak

In order to implement my equilibrium profiles for the magnetic field (described in section 2.1), I first had to rewrite them under the M3DC1 form with ψ and B_z , to calculate analytically their first and second derivatives in x and y and then to insert them into the code. A random perturbation is applied to the scalar fields at $t = 0$ and then the time advance equations are used until the instability with the largest growth rate dominates all the others. At that time, we can calculate the growth rate with the time derivative of the total kinetic energy, which is in a very good approximation the kinetic energy of the mode with the largest growth rate :

$$\gamma = \frac{1}{2} \frac{d}{dt} \log (KE) = \frac{1}{2} \frac{d}{dt} \log \left(\int \frac{1}{2} \rho \vec{v}^2 d\vec{r} \right)$$

We can see the time evolution of the growth rate calculated this way during a simulation on figure 12. It is noisy at the beginning and then takes a stable value after a certain time.

Since the instability is highly localized at the singular surface, the mesh size had to be smaller in the vicinity of r_s . This was performed by refining an initial uniform mesh with the following parameters : (1) the radius at which the mesh should be finer (r_s in our case), (2) the mesh size in the outer region (H), (3) the mesh size in the inner region (h) and the width on which the transition from h to H should be done (W). You can see a typical refined mesh and the parameters on figure 6. A zoom on the finer mesh region at the singular surface can be seen on figure 11.

The convergence of the growth rate on the mesh size was checked with a series of meshes for which W and h/H were fixed and H was successively lowered. The convergence with the time step was checked as well (figure 13).

5 Benchmark

As explained before, M3DC1 only allows us to calculate growth rates for the most unstable mode. For a given n , it occurs for the lowest m such as $q = m/n$ has a solution. Higher m modes are stabilized by the line bending potential energy term which goes up with m . Since our q profile is always higher than one, we studied the $m = 2, n = 1$ mode. The comparison between growth rates coming from the asymptotic matching method and the M3DC1 code can be seen in figure 7. As we know, the asymptotic matching method is no longer accurate for a resistivity that gets too large, as this is the small parameter on which the method is based. We can for example estimate the maximal resistivity at about 10^{-5} for $\beta = 0.05$ by looking at figure 9. On the other side, the M3DC1 simulations get more demanding for lower resistivity, because the instability becomes more localized and thus needs a finer mesh at the singular surface. The minimal resistivity is determined by the maximal number of nodes in the mesh allowed by the random access memory available on the machines we were using. This limit was found to be at around $\eta = 10^{-7}$. This gave us a resistivity range on which we could perform the benchmark, as we can see on figure 7. The agreement ranges from 10 to 25% for the results coming from the full 6-fields resolution from M3DC1 while it goes from 1 to 5% for the results of the 4-fields reduced resolution of M3DC1. The convergence with the time step was also better with the 4-fields version of the simulations, as we can see on figure 13. This could point out a bug in the equations for χ and p , the two fields removed with this version. This would also mean that the 4-fields reduced system is sufficient to describe accurately the physics of the problem. Since the physics removed from the full system is the compressible motion in the plane (x, y) associated with χ , the motion in this plane should be almost incompressible. This is coherent with the fact that the instability grows on a time scale which is hybrid between Alfvénic and resistive. We can see in figure 8 that the velocity of the fast magnetosonic waves is much higher

than the Alfvén waves when we look at propagation nearly perpendicular to \vec{B} . In our case, the equilibrium magnetic field is mostly in the z direction, and thus fast waves propagate on a time scale much shorter than Alfvén waves in the (x, y) plane. These fast waves have thus time to assure pressure equilibrium, and the motion can be considered quasi incompressible in the (x, y) plane.

The discrepancy occurring for low η can be explained by the fact that the solution gets too localized at the singular surface and thus we reach the largest mesh possible with the memory available and we cannot guarantee spatial convergence for these points.

Note that, while the outer solution was in both cases obtained with my code, we used two different solutions for the inner region. The first one is the numerical one from Ref. [16] and described in the section “Inner region” of this report. The second one is an analytical one, true only in the limit of $Q \ll 1$ where Q is the scaled growth rate[8]. As we can see on figure 7, the results from M3DC1 tend to confirm the first solution against the second. This is interesting because the analytical solution is the one which is used in most papers[9] and it would be interesting to compare the results of these papers with the ones obtained with the numerical inner solution from Ref. [16]

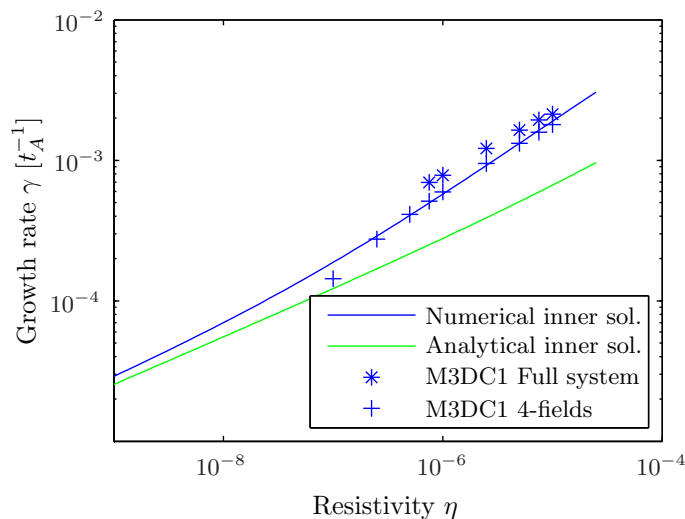


Figure 7: Growth rate versus resistivity for typical parameters ($r_s = 0.45$, $r_0 = 0.5$, $k = 0.1$, $m = 2$, $n = 1$)

6 Conclusion

The cylindrical tokamak, an approximation of the toroidal tokamak in the large aspect ratio limit, was studied both analytically and numerically. We were interested in the linear stability of typical tokamak equilibria against instabilities mostly driven by resistive effects. We solved thus the resistive magnetohydrodynamics equations.

The analytical solution was performed with an asymptotic matching method, using the resistivity as the small parameter. This allowed us to separate the domain into an ideal outer region and a narrow resistive inner region located at a certain radius called the singular surface. The matching between the solutions in these two regions gave us the growth rate of the instability.

The numerical solution was obtained with a finite elements code called M3DC1. A random perturbation superposed on the equilibrium was given as the initial condition and the system was integrated in time with an implicit algorithm. After a certain time, the solution was dominated by

the mode with the largest growth rate, which is the one we were interested in. We could compute the growth rate with the time derivative of the kinetic energy.

In the end we compared the growth rates obtained with both methods and a fairly good agreement was shown for a certain reduced version of M3DC1 in which the compressible part of the motion was removed. This confirms the prediction that the motion is mostly incompressible for these instabilities, and casts doubt on the accuracy of the treatment of the compressible part of the equations in M3DC1.

The extended capabilities of M3DC1 offer a large variety of possible follow-ups for this work. A study on the equilibrium parameters and on different equilibrium profiles would be interesting. We could study the saturation of the same instability with the non-linear option of M3DC1. A non-linear analytic solution exists as well and the asymptotic matching code I wrote would be useful to implement it since the non-linear solution needs some results from the linear treatment. Finally, the instability could be studied with M3DC1 in a more realistic toroidal geometry and the results could be compared with experimental data.

References

- [1] D. Biskamp. *Magnetic Reconnection in Plasmas*. Cambridge Monographs on Plasma Physics, 2000.
- [2] J. DeLucia S. C. Jardin A. H. Glasser. Resistive stability of the cylindrical spheromak. *The Physics of Fluids*, 1984.
- [3] B.-L. Tan G.-L. Huang. Neoclassical bootstrap current in solar plasma loops. *Astronomy and Astrophysics*, 2006.
- [4] S. C. Jardin J. Breslau, N. Ferraro. Some properties of the m3d-c1 form of the three-dimensional magnetohydrodynamics equations. *Physics of Plasmas*, 2009.
- [5] X. S. Li J. W. Demmel, J. R. Gilbert. An asynchronous parallel supernodal algorithm for sparse gaussian elimination. *Matrix Anal. Appl.*, 1999.
- [6] S. C. Jardin. *Computational Methods in Plasma Physics*. CRC Press, 2010.
- [7] S. C. Jardin. Review of implicit methods for the magnetohydrodynamic description of magnetically confined plasmas. *Journal of Computational Physics*, 2011.
- [8] A. H. Glasser J. M. Greene J. L. Johnson. Resistive instabilities in general toroidal plasma configurations. *Nuclear Fusion*, 1982.
- [9] L.-J. Zheng M. Furukawa, S. Tokuda. A numerical matching technique for linear resistive magnetohydrodynamics modes. *Physics of Plasmas*, 2010.
- [10] S. C. Jardin N. M. Ferraro. Calculations of two-fluid magnetohydrodynamic axisymmetric steady-states. *Journal of Computational Physics*, 2009.
- [11] W. A. Newcomb. Hydromagnetic stability of a diffuse linear pinch. *Annals of Physics*, 1960.
- [12] C. M. Bender S. A. Orszag. *Advanced Mathematical Methods for Scientists and Engineers*. McGRAW-HILL, 1978.
- [13] N. Ferraro S. C. Jardin, J. Breslau. A high-order implicit finite element method for integrating the two-fluid magnetohydrodynamic equations in two dimensions. *Journal of Computational Physics*, 2007.
- [14] H. P. Furth P. H. Rutherford H. Selberg. Tearing mode in the cylindrical tokamak. *The Physics of Fluids*, 1973.
- [15] M. S. Chance H. P. Furth A. H. Glasser H. Selberg. Ideal- and resistive-mhd stability of one-dimensional tokamak equilibria. *Nuclear Fusion*, 1982.
- [16] A. H. Glasser S. C. Jardin G. Tesaro. Numerical solution of the resistive magnetohydrodynamic boundary layer equations. *The Physics of Fluids*, 1984.
- [17] G. Hall J. M. Watt. *Modern Numerical Methods for Ordinary Differential Equations*. Modern Numerical Methods for Ordinary Differential Equations, 1976.
- [18] R. B. White. *The Theory of Toroidally Confined Plasmas*. Imperial College Press, 2001.

A Appendix

A.1 “Frozen in” theorem

We can see this property by going back to the induction equation :

$$\frac{\partial \vec{B}}{\partial t} = \nabla \times (\vec{v} \times \vec{B} - \eta \nabla \times \vec{B}) = \nabla \times (\vec{v} \times \vec{B}) + \eta \Delta \vec{B} \quad (26)$$

where we have used $\nabla \cdot \vec{B} = 0$. In the ideal case ($\eta = 0$), we get

$$\frac{\partial \vec{B}}{\partial t} = \nabla \times (\vec{v} \times \vec{B})$$

We integrate over a given surface $S(t)$ that moves with the plasma,

$$\int_{S(t)} \frac{\partial \vec{B}}{\partial t} \cdot \vec{d}s = \int_{S(t)} (\nabla \times (\vec{v} \times \vec{B})) \cdot \vec{d}s = \int_{C(t)} (\vec{v} \times \vec{B}) \cdot \vec{d}l = \int_{C(t)} (\vec{d}l \times \vec{v}) \cdot \vec{B} \quad (27)$$

with $C(t)$ the contour of $S(t)$. If we define the flux function Φ as

$$\Phi(t) = \int_{S(t)} \vec{B} \cdot \vec{d}s$$

then the time derivative of Φ has one contribution coming from the time variation of the magnetic field and one coming from the time variation of the surface :

$$\frac{d\Phi}{dt} = \int_{S(t)} \frac{\partial \vec{B}}{\partial t} \cdot \vec{d}s + \int_{C(t)} (\vec{v} \times \vec{d}l) \cdot \vec{B}$$

($\vec{v} \times \vec{d}l$ is the area swept by $\vec{d}l$ per unit time while being convected by the velocity field). It is clear from equation 27 that these two contributions cancel each other, giving finally

$$\frac{d\Phi}{dt} = 0$$

In summary, the magnetic flux on a surface moving with the fluid is constant in time in ideal MHD, or in other words the magnetic field lines are frozen into the plasma.

A.2 Parity conservation

We can see the parity conserving nature of equation 14 by operating the parity transformation ($x \rightarrow -x$)

$$\frac{d^2}{dx^2} \begin{pmatrix} \Psi_1(-x) \\ \Psi_2(-x) \\ \Psi_3(-x) \end{pmatrix} = \begin{pmatrix} Q & xQ & 0 \\ x/Q & x^2/Q & -(E+F)/Q^2 \\ x/Q & -(G-E/F)Q & x^2/Q + (G+1)Q \end{pmatrix} \begin{pmatrix} \Psi_1(-x) \\ \Psi_2(-x) \\ \Psi_3(-x) \end{pmatrix}$$

Explicit calculation shows that if we suppose $\Psi_1(-x) = \Psi_1(x)$, then we must have $\Psi_2(-x) = -\Psi_2(x)$ and $\Psi_3(-x) = -\Psi_3(x)$ in order for the parity transformed system to be equivalent to the original one. On the contrary, if we suppose $\Psi_1(-x) = -\Psi_1(x)$, then we must have $\Psi_2(-x) = \Psi_2(x)$ and $\Psi_3(-x) = \Psi_3(x)$.

A.3 Figures

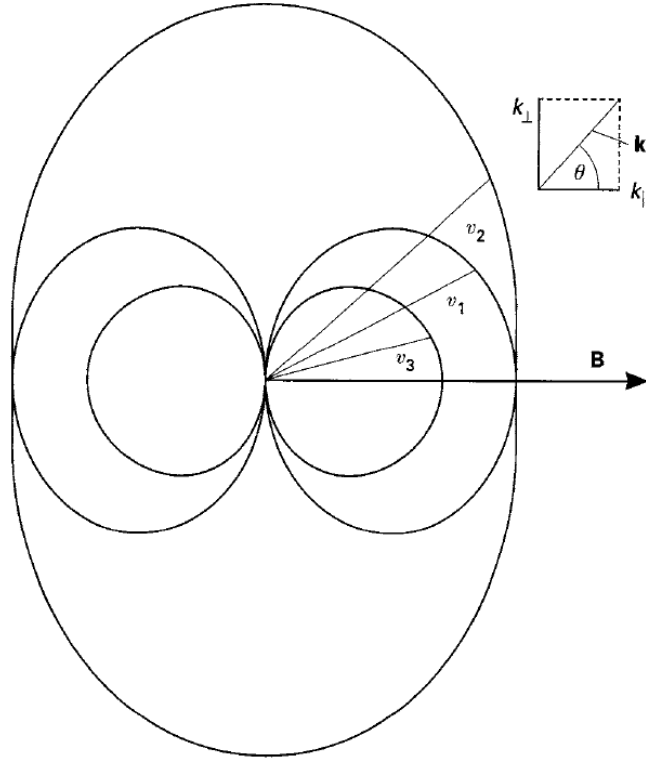


Figure 8: Phase velocity of the three types of MHD waves : (1) Alfvén wave (2) fast magnetosonic waves (3) slow magnetosonic waves in function of the angle between the equilibrium magnetic field and \vec{k} [1]

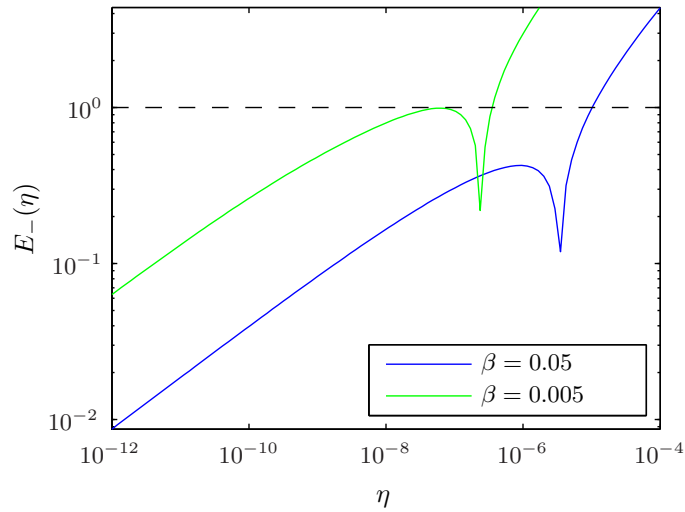


Figure 9: $E_+(\eta)$ for typical parameters ($r_s = 0.45$, $r_0 = 0.5$, $k = 0.1$, $m = 2$, $n = 1$)

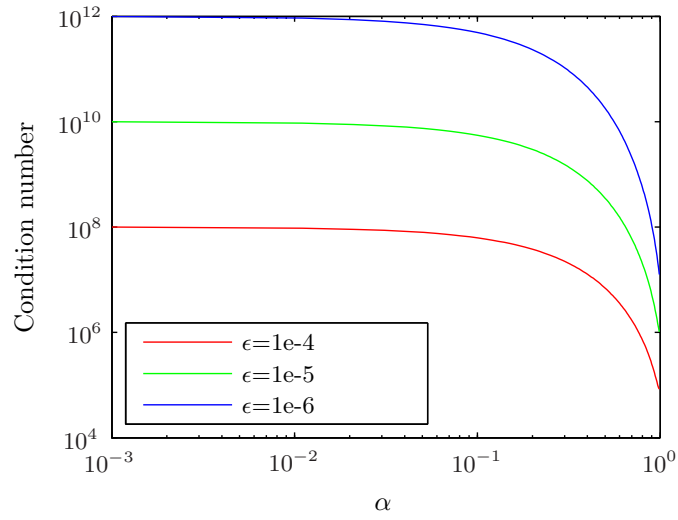


Figure 10: Condition number of the matrix A defined in equation 22 in function of the normalized pressure gradient α

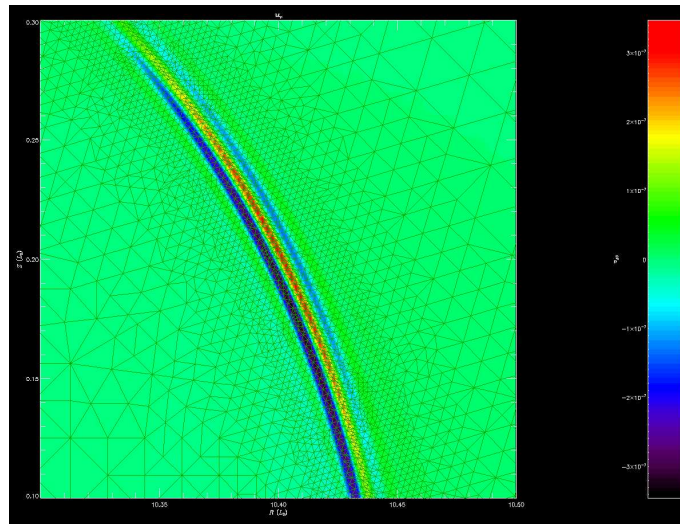


Figure 11: Zoom on the singular surface where the mesh had to be refined because of the sharp spatial dependence of the field. The field shown is the radial velocity.

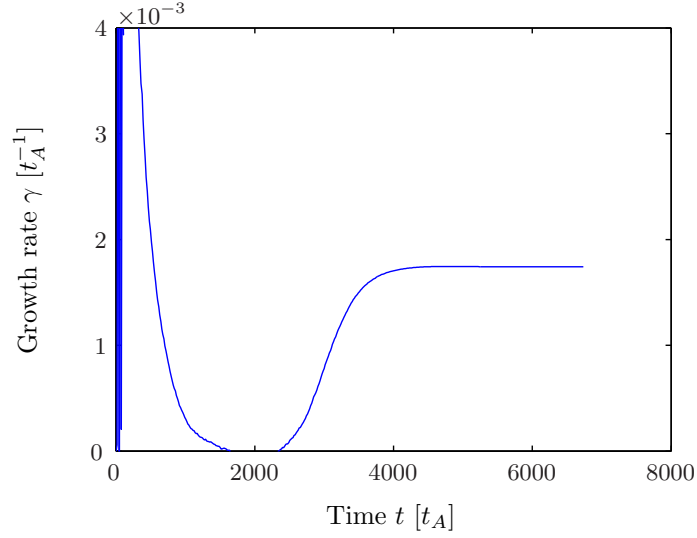


Figure 12: Time evolution of the growth rate during a M3DC1 simulation

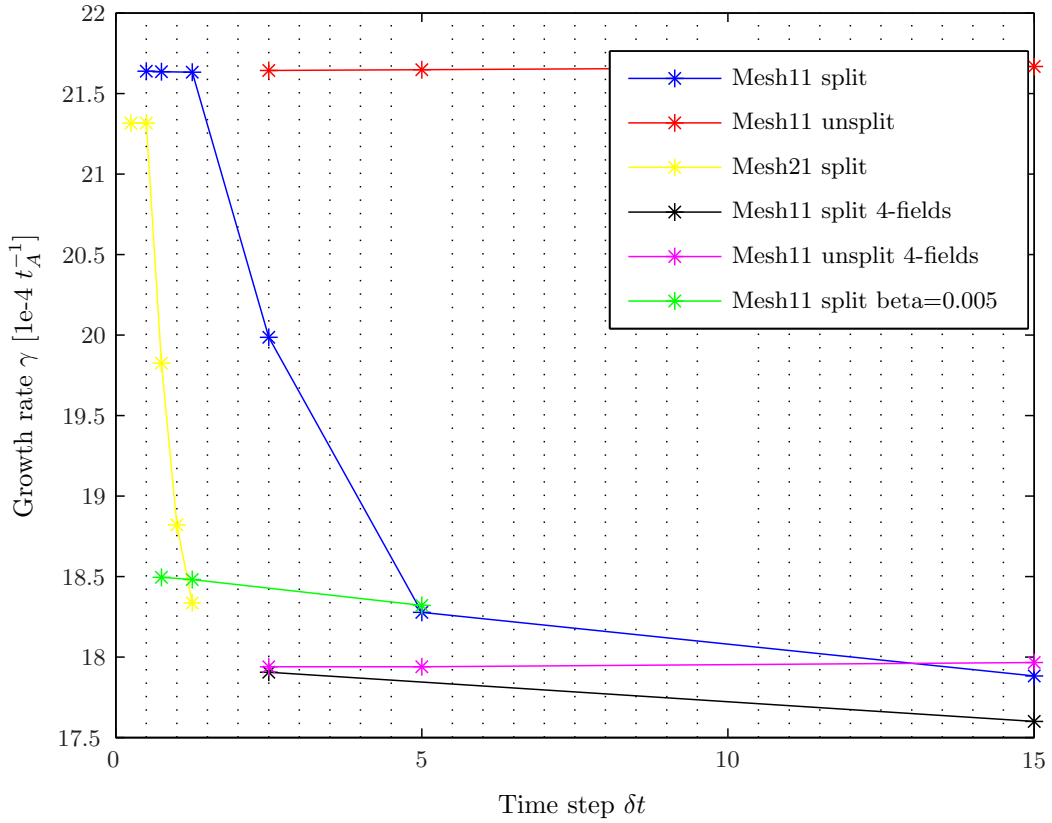


Figure 13: Convergence of the growth rate with the time step for $\eta = 10^{-5}$. All lines are for $\beta = 0.05$ except the green one which is for $\beta = 0.005$. The asymptotic matching value for the growth rate for $\beta = 0.05$ is 18.9 and for $\beta = 0.005$ is 15.2. Mesh11 is a mesh of around 10^4 nodes while mesh21 has around $3 \cdot 10^4$ nodes. The converge seems better for lower β and for numvar=2.